symmetry

IMPACT FACTOR 2.7

CITESCORE 4.9

Article

Excitation Function of Freeze-Out Parameters in Symmetric Nucleus–Nucleus and Proton–Proton Collisions at the Same Collision Energy

Murad Badshah, Abd Haj Ismail, Muhammad Waqas, Muhammad Ajaz, Mateen Ullah Mian, Elmuez A. Dawi, Muhammad Adil Khan and Atef AbdelKader

MDPI

https://doi.org/10.3390/sym15081554

symmetry

MDPI

Article

Excitation Function of Freeze-Out Parameters in Symmetric Nucleus–Nucleus and Proton–Proton Collisions at the Same Collision Energy

Murad Badshah [1], Abd Haj Ismail [2,3,*], Muhammad Waqas [4,*], Muhammad Ajaz [1,*], Mateen Ullah Mian [5], Elmuez A. Dawi [2,3], Muhammad Adil Khan [5] and Atef AbdelKader [2,3]

1 Department of Physics, Abdul Wali Khan University Mardan, Mardan 23200, Pakistan
2 Department of Mathematics and Science, Ajman University, Ajman P.O. Box 346, United Arab Emirates
3 Nonlinear Dynamics Research Center (NDRC), Ajman University, Ajman P.O. Box 346, United Arab Emirates
4 School of Mathematics, Physics and Optoelectronic Engineering, Hubei University of Automotive Technology, Shiyan 442002, China
5 Department of Physics, Islamia College Peshawar, Peshawar 25120, Pakistan
* Correspondence: a.hajismail@ajman.ac.ae (A.H.I.); 20220073@huat.edu.cn (M.W.); ajaz@awkum.edu.pk (M.A.)

Abstract: We analyze the transverse momentum (p_T) spectra of π^+, π^-, K^+, K^-, p, $\bar{p}$, Λ, $\bar{\Lambda}$, Ξ, $\bar{\Xi}$, Ω^-, $\bar{\Omega}^+$ or $\Omega^- + \bar{\Omega}^+$ in different centrality intervals in gold–gold (Au–Au) and lead–lead (Pb–Pb) symmetric collisions at 200 GeV and 2.76 TeV, respectively, by Tsallis–Pareto-type function. Proton–proton collisions at the same centre of mass energies are also analyzed for these particles to compare the results obtained from these systems. The present work extracts the effective temperature T, non-extensivity parameter (q), the mean transverse momentum spectra ($\langle p_T \rangle$), the multiplicity parameter (N_0), kinetic freeze-out temperature (T_0) and transverse flow velocity (β_T). We reported a plateau structure of p_T, T, T_0, β_T, p_T and q in central collisions. Beyond the plateau region, the excitation function of all the above parameters decreases towards the periphery, except q, which has a reverse trend. The multiplicity parameter is also extracted, which is found to be decreasing towards the periphery from the central collisions. In addition, we observed that the excitation function of pp collisions is nearly the same to that of the most peripheral symmetric nucleus–nucleus collisions at the same colliding energy. Throughout the analyses, the same multiplicity parameters for particles and their antiparticles have been reported, which show the symmetric production of particles and their antiparticles.

Keywords: identified particles; strange particles; effective temperature; non-extensivity parameter; centrality bins; multiplicity parameter; kinetic freeze-out stage; multiple freeze-out scenario

Citation: Badshah, M.; Haj Ismail, A.; Waqas, M.; Ajaz, M.; Mian, M.U.; Dawi, E.A.; Adil Khan, M.; AbdelKader, A. Excitation Function of Freeze-Out Parameters in Symmetric Nucleus–Nucleus and Proton–Proton Collisions at the Same Collision Energy. *Symmetry* **2023**, *15*, 1554. https://doi.org/10.3390/sym15081554

Academic Editors: Jorge Segovia and Sergei D. Odintsov

Received: 10 June 2023
Revised: 25 July 2023
Accepted: 3 August 2023
Published: 8 August 2023

1. Introduction

It is well known that ordinary matter contains nucleons, protons and neutrons, the colourless bound states of quarks [1], and gluons [2]. Quarks and gluons do not exist freely in nature, a phenomenon called quark confinement. However, the developments in quantum chromodynamics (QCD) and experiments have shown that the collisions of heavy nuclei, particularly Au–Au and Pb–Pb collisions, at relativistic energies leads to the formation of a very hot and highly dense state of matter, where quarks and gluons are assumed to be asymptotically free, called quark gluon plasma (QGP) [3–7]. The study of QGP has revealed that the properties of QGP resemble the properties of the early universe, particularly the enormous temperature and density [8–12]. When two Lorentz-contracted nuclei collide with each other at relativistic energies, they are most likely to form QGP. Due to the pressure gradient and to attain equilibrium with the surrounding, the matter expands, which cools it down approximately adiabatically [3,13] and eventually starts hadronization. The unstable hadrons produced due to hadronization decay into stable hadrons and fly off toward the detectors fixed around the beam axis.

During the evolution of the QGP, the two freeze-out stages, the chemical freeze-out stage and the thermal or kinetic freeze-out stage, are very significant to have true knowledge about the nature of the QGP. The chemical freeze-out stage is the stage at which the inelastic interactions among the constituents of the fireball stop; hence no new particle production will take place after this stage. The temperature at this stage is called the chemical freeze-out temperature [14–16]. The stage at which the elastic interactions among the constituents of the fireball cease and hence no exchange of energy and momentum etc., takes place among them is known as the thermal or kinetic freeze-out stage. The temperature at this stage is known as thermal or kinetic freeze-out temperature [17,18]. Kinetic freeze-out is the last but not the least stage in the evolution process, and the particles spectra are fixed at this stage, which carries the crucial information of the final state particles.

Transverse momentum (p_T) distributions are the best tools to extract information about the degree of the thermal excitation function and the collective expansion of the system, and one can use various hydrodynamical and statistical models for this purpose. These models include but are not limited to the non-extensive Tsallis distribution [19–23], the Hagedorn model with embedded transverse flow velocity [24], the standard distribution with a single and two-component temperatures [25] and the Blast Wave Model [26–30]. Each of these models depends on a different combination of free parameters and has its own regime of applicability. The parameters, namely the effective temperature, kinetic freeze-out temperature, chemical freeze-out temperature and kinetic freeze-out volume can be extracted from these models. Among them, the kinetic freeze-out temperature is controversial in the literature. For instance, Refs. [31–33] shows a decreasing trend of the kinetic freeze-out from central collisions toward the periphery while Refs. [34,35] show the opposite behaviour, and Ref. [36] shows the invariant behaviour of the effective temperature from central to peripheral collisions and that the degree of thermal excitation does not change from central to peripheral collisions.

This study provides insights into the freeze-out process of the particles, and in fact, freezing-out of the particles is different in different studies. Ref. [37] shows a single freeze-out for all the particles where a single set of parameters is used for the particles; the same reference also shows separate sets of parameters for the light (identified) and heavy (strange) particles which give a double kinetic freeze-out scenario. In Ref. [38], a triple kinetic freeze-out scenario is observed where the identified, single-strange and multi-strange particles have separate sets of parameters. These two issues discussed above are in fact open questions in the community which need to be solved.

Before going to the next section, we would like to point out that the study of high temperature and high density is very important because these are the possible regions for QGP. The higher density and higher temperature is possible at relativistic energies as well as in heavy nuclear (such as Au–Au or Pb–Pb) reactions rather than hadronic reactions. In this work, we will study Au–Au and Pb–Pb symmetric collisions at 200 GeV and 2.76 TeV, respectively. This work searches for the QGP formation in the possible regions of central collisions. However, we also presented the study of pp collisions at 200 GeV and 2.76 TeV in order to compare the thermodynamic properties of pp collisions with that of AA collisions.

The rest of the paper has been organized as follows: Section 2 deals with the description of the method and formalism, while Section 3 describes the results and discussion, and in Section 4 we concluded our work.

2. The Method and Formalism

The transverse momentum distribution of the outgoing particles encodes important information about the freeze-out stage of the system produced in the relativistic heavy ion collision. Therefore, the p_T distribution is assumed to be the best observable in studying the true nature of QGP and its different stages of evolution . The Boltzmann–Gibbs exponential

function, given in Equation (1), has been used for decades to describe the p_T spectra of outgoing particles.

$$f(E) \propto \exp\left(-\frac{E-\mu}{T}\right), \tag{1}$$

where E denotes energy, μ is the chemical potential, and T is the corresponding temperature. However, the Boltzmann–Gibbs exponential function fails at $p_T > 3$ GeV/c, i.e., at high p_T regimes. This is because, in this regime, particle production has been governed by different physical processes and is assumed to be governed by non-thermal and non-equilibrium perturbative QCD processes. Instead of an exponential function, a power law distribution is more promising in such a regime [39]. To formulate the power law distribution, the Boltzmann–Gibbs theory is generalized in the context of non-extensive statistics, i.e., the statistical picture has been modified, and what has been obtained in this generalization is called the non-extensive Tsallis–Pareto distribution function [40,41]. The function used to describe p_T spectra of the particles in their simplest form is given in Equation (2) or Equation (3).

$$f(E, q, T, \mu) = \left[1 + \frac{q-1}{T}(E-\mu)\right]^{-\frac{1}{q-1}} \tag{2}$$

At mid-rapidity, use $\mu = m_0$, where m_0 denotes the rest mass of the outgoing hadron, also at this rapidity $E = m_T = \sqrt{{p_T}^2 - {m_0}^2}$, making these substitutions one can obtain,

$$\frac{d^2N}{2\,\pi\,p_T\,dp_T\,dy} = A\,m_T\left[1 + \frac{q-1}{T}(m_T - m_0)\right]^{-\frac{q}{(q-1)}} \tag{3}$$

where T denotes the effective temperature. Generally, $T = T_0 + m_0\langle\beta_T\rangle$ where T_0 is the kinetic freeze-out temperature and $\langle\beta_T\rangle$ is the mean transverse flow velocity. q is called the non-extensivity parameter, the system's thermalization level increases if q approaches unity. At q = 1, the Tsallis–Pareto function approaches the Boltzmann–Gibbs exponential function, A is the normalization constant and is given as $A = \frac{C_y g V}{(2\pi)^3}$. Where C_y denotes the shorthand notation of the correcting factor for the data recorded in the experiments, g represents the degeneracy factor, V is the kinetic freeze-out volume of the outgoing particles, $m_T = \sqrt{{p_T}^2 - {m_0}^2}$, is the transverse mass, and m_0 represents the rest mass of the outgoing particle. For pseudo rapidity differential yields, $C_y = \frac{m_T}{p_T}$ and for the rapidity differential yield, $C_y = 1$; we will be dealing with the latter case, as we are using rapidity yield in Equation (3).

In cases where the hard process ($p_T > 3$ GeV/c) is taken into account, then the power law distribution is found to be more prominent and is given as

$$f(p_T) = \frac{1}{N}\frac{dN}{dp_T} = Ap_T\left(1 + \frac{p_T}{p_0}\right)^{-n}, \tag{4}$$

where A denotes the normalization constant and n and p_0 are the free parameters.

We can use the superposition principle when the hard scattering is involved which is as follows:

$$f(p_T) = \frac{1}{N}\frac{dN}{dp_T} = kf_S(p_T) + (1-k)f_H(p_T). \tag{5}$$

where f_H and f_S represent soft and hard processes and k is the contribution fraction of the soft process to the hard process. The contribution of the soft component is from 0 to 2 or 3 GeV/c or a little more, while the hard component contributes to the whole p_T region. The soft component is the main contributor in the low p_T region, and in high p_T, the only contributor is the hard component and it comes from the inverse power law.

In this work, we have used the soft component of the model only, but we discussed the hard model in order to understand the whole phenomenology in case the hard component is included. It should also be noted that if the hard component is included, despite the soft component playing a main role in low p_T region, the hard component covers the whole p_T region.

3. Results and Discussion

Figures 1 and 2 represent the p_T spectra of light (π^+, π^-, K^+, K^-, p and $\bar{p}$) and heavy (Λ, $\bar{\Lambda}$, Ξ, $\bar{\Xi}$, Ω^- and $\bar{\Omega}^+$ or $\Omega^- + \bar{\Omega}^+$. Different symbols represent the experimental data while the solid lines are our fit lines obtained through fitting by using Equation (3). The spectra are scaled by some factors, listed in Table 1, to avoid overlapping and enhance their visibility. Each plot has a Data/Fit panel at its bottom, presenting the fitting quality. The values of different parameters, including T, q, $\langle p_T \rangle$, N_0, χ^2 and NDF have been obtained from fitting and are listed in Table 1. Where NDF represents the number of degrees of freedom and χ^2 is given as [34]

$$\chi^2 = \sum_i \frac{(R_i^{Exp} - R_i^{Theor})^2}{\epsilon^2}. \tag{6}$$

χ^2 is the deviation of the fit line from the experimental data points providing the fit quality. In Equation (6), R_i^{Exp} denotes the experimentally measured data, ϵ is the uncertainty in this measurement and R_i^{Theor} denotes the values calculated through our model.

Figure 1a,b,c,d,e,f represent the event centrality-dependent double differential p_T spectra of $\pi^+, \pi^-, K^+, K^-, p$ and $\bar{p}$, respectively, at $\sqrt{s_{NN}}$ = 200 GeV in the Au–Au collision measured by PHENIX at RHIC [42]. The data for these particles have been analyzed at all available centrality events of 0–5%, 5–10%, 10–15%, 15–20%, 20–30%, 30–40%, 40–50%, 50–60%, 60–70%, 70–80% and 80–92%. Similarly, Figure 1g,h,i,j,k represent the p_T distribution of Λ, $\bar{\Lambda}$, Ξ, $\bar{\Xi}$, $\Omega^- + \bar{\Omega}^+$, respectively, measured by STAR collaboration at RHIC [43], at centrality events of 0–5%, 10–20%, 20–40%, 40–60% and 60–80%. The symbols with different colours show different centrality bins and the solid lines are the fit results. One can easily see that the fit results of Equation (3) agree with the experimental data.

Figure 2a,b,c,d,e,f represent the p_T distribution of $\pi^+, \pi^-, K^+, K^-, p$ and $\bar{p}$, respectively, at $\sqrt{s_{NN}}$ = 2.76 TeV in the Pb–Pb collision measured by ALICE at LHC [44]. The analyses for these particles have been carried out for 0–5%, 5–10%, 10–20%, 20–30%, 30–40%, 40–50%, 50–60%, 60–70%, 70–80% and 80–92% centrality bins. Similarly, panel (g), (h), (i), (j) and (k) of this figure represent the p_T distribution of Λ, $\bar{\Lambda}$, Ξ, $\bar{\Xi}$, Ω^- and $\bar{\Omega}^+$, respectively, measured by ALICE at LHC [45,46] in 0–10%, 10–20%, 20–40%, 40–60% and 60–80% centrality events. Different symbols with colours denote different centrality bins, while the solid lines show our fit results using Equation (3). One can see that Equation (3) agrees with the experimental data.

In addition to the A–A collision, we also analyzed the p–p collision for the same particles and at the same energies. Figure 3a represents the p_T distribution of different light and heavy hadrons in p–p collisions at $\sqrt{s}$ = 200 GeV measured by STAR collaboration at RHIC [47,48], while Figure 3b represents the p_T spectra of light hadrons at $\sqrt{s}$ = 2.76 TeV measured by CMS at LHC [49]. Figure 3a has two types of distributions along the y-axis, the distribution, $\frac{1}{(2\pi p_T)} \frac{d^2N}{dydp_T}$ is for light particles and the distribution, $\frac{1}{(2\pi N_{ev} p_T)} \frac{d^2N}{dydp_T}$ is for heavy particles.

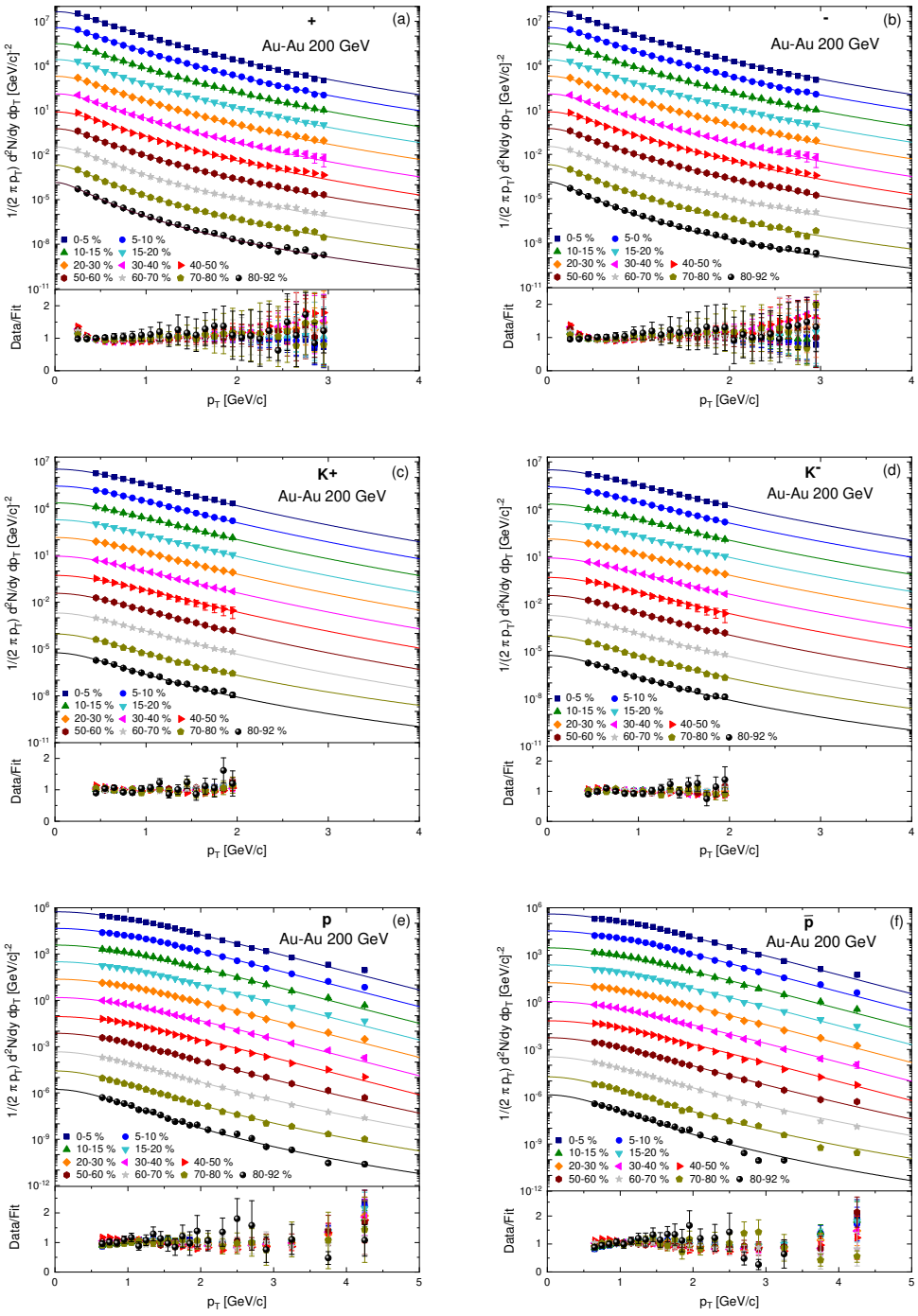

Figure 1. *Cont*.

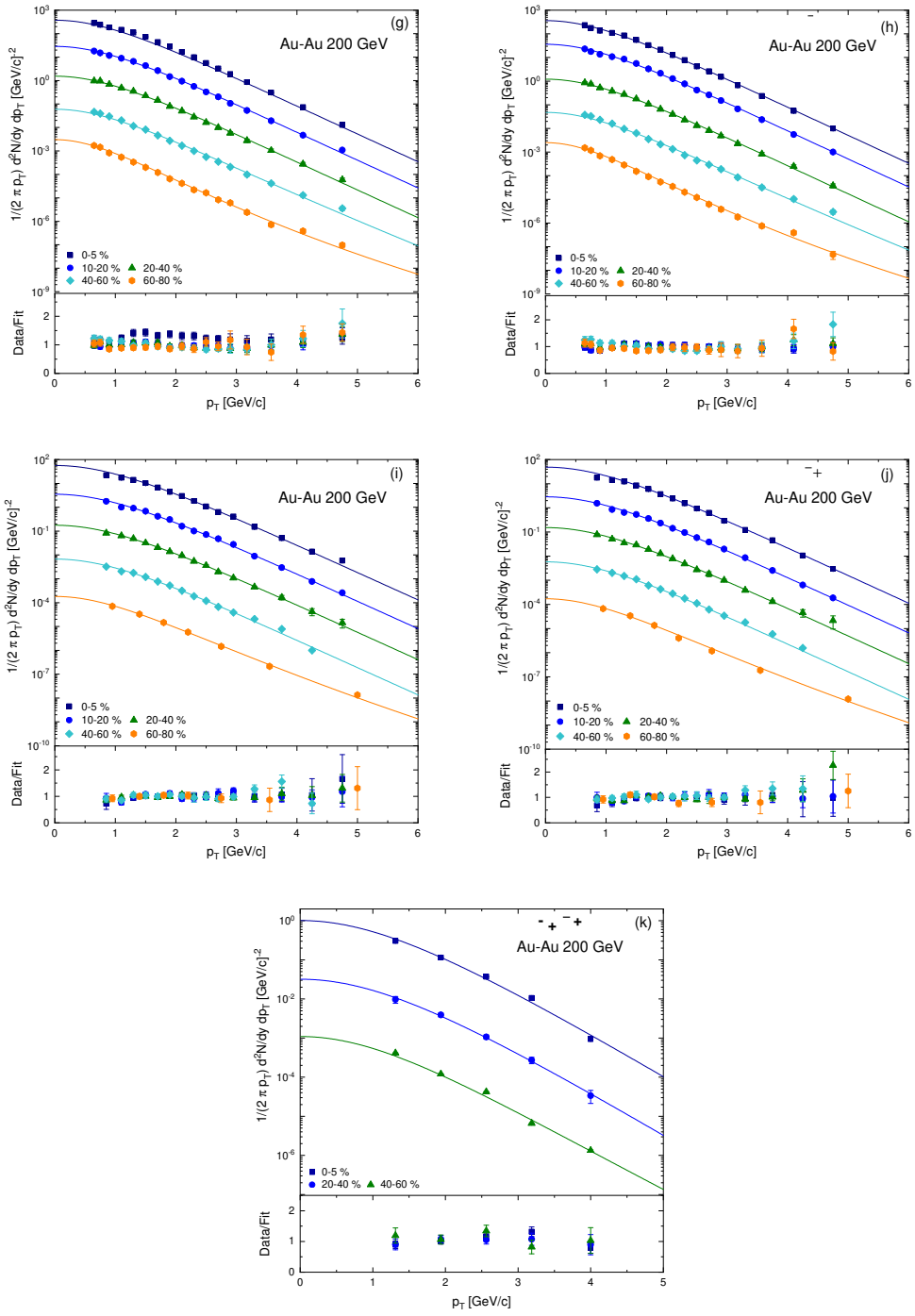

Figure 1. Plots (**a**–**k**) represent the event centrality-dependent double differential p_T spectra of light particles at $|\eta| < 0.35$ measured by PHENIX Collaboration at RHIC [42] and heavy hadrons, at $|y| < 1$ for Λ and $\bar{\Lambda}$ and $|y| < 0.5$ for Ξ, $\bar{\Xi}$ and $\Omega^- + \bar{\Omega}^+$ measured by STAR at RHIC [43] at $\sqrt{s_{NN}}$ = 200 GeV in Au–Au collision. The data for these particles have been analyzed at all available centrality events indicated in each plot. Different symbols with different colours are used for different centralities, while the solid lines are the results of our fit by using Equation (3). Each plot has the Data/Fit ratio at its bottom, which shows the fit quality.

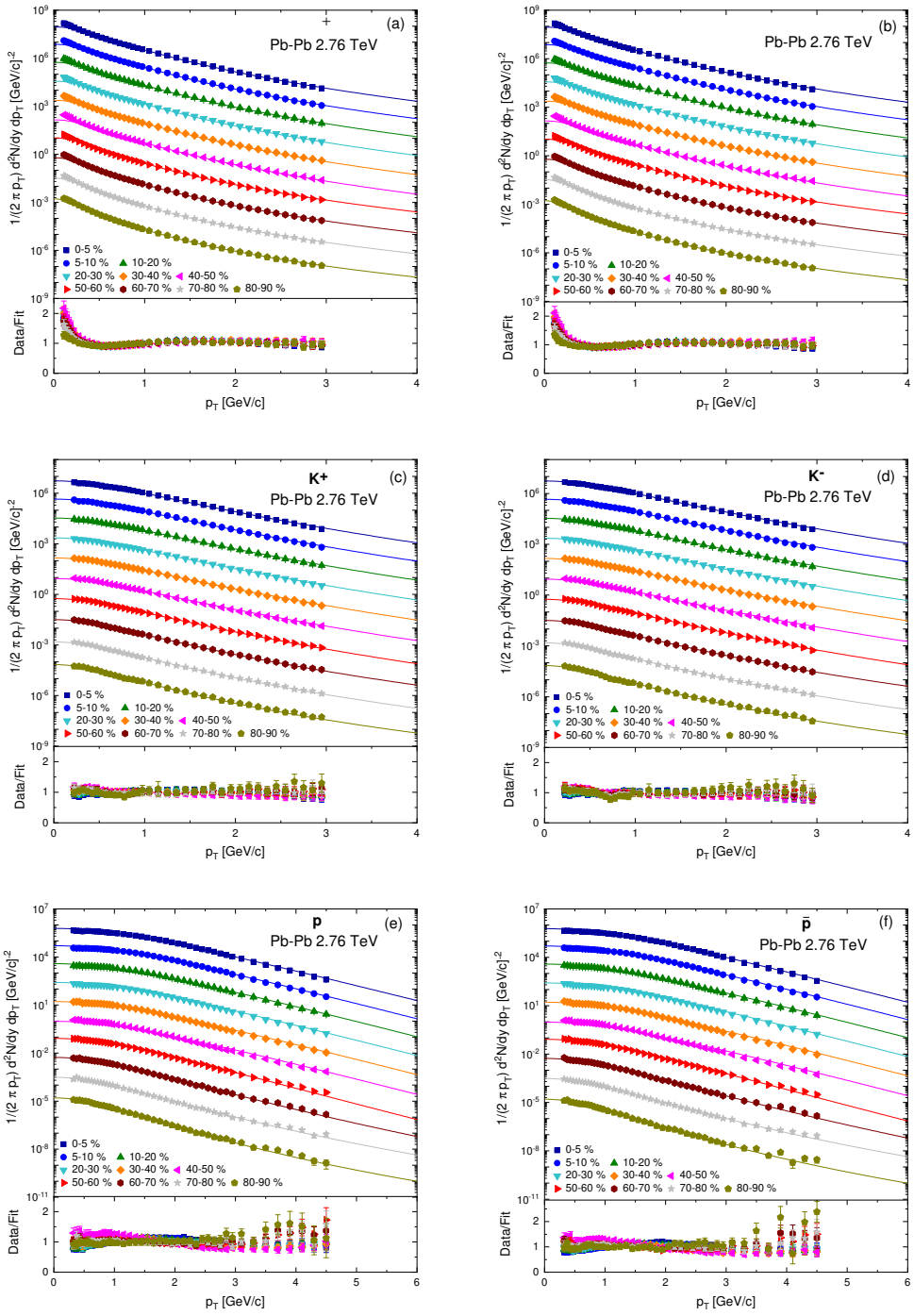

Figure 2. *Cont.*

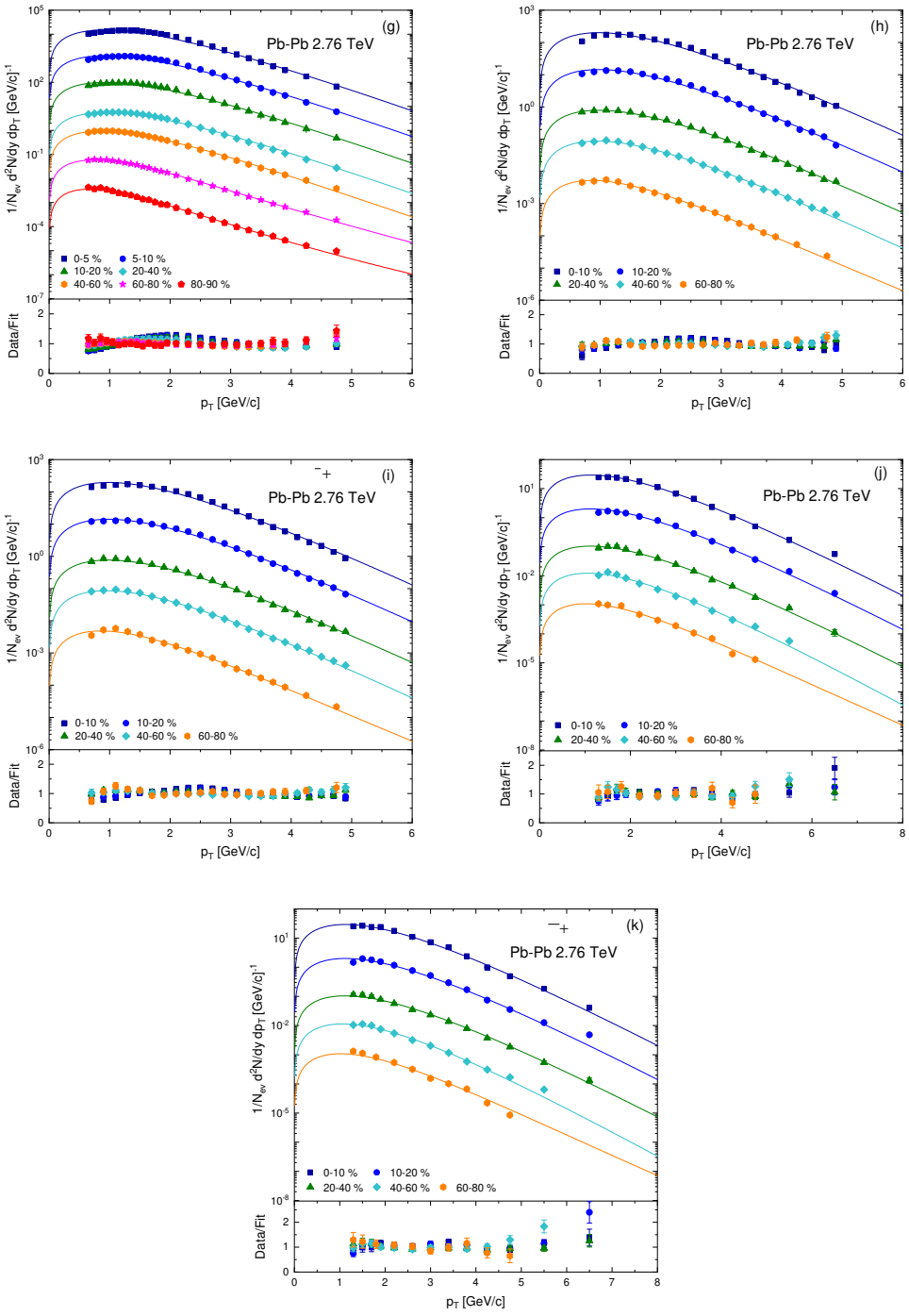

Figure 2. Plots (**a**–**k**) represent the event centrality-dependent double differential p_T spectra of different light and heavy hadrons at $\sqrt{s_{NN}}$ = 2.76 TeV in Pb–Pb collision measured by ALICE Collaboration at LHC at $|y| < 0.5$ [44–46]. The symbols are used for experimental data and curves are our fit results by Equation (3).

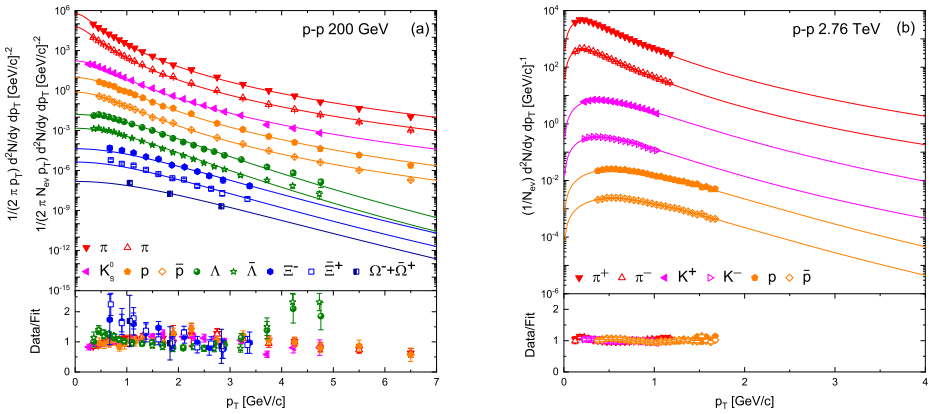

Figure 3. Transverse momentum distribution of (**a**) light and heavy particles in p–p collision at $\sqrt{s} = 200$ GeV measured by STAR at RHIC at $|y| < 0.5$ [47,48] and (**b**) light particles in p–p collision at $\sqrt{s} = 2.76$ TeV measured by CMS Collaboration at LHC at $|y| < 1$ [49]. The symbols are used to represent the experimental data of different particles, and solid curves are our fit results.

Table 1. Values of free parameters T and q, N_0, $\langle p_T \rangle$ and χ^2/NDF extracted from the Tsallis–Pareto-type function given in Equation (3).

Collision	Particle	Centrality	Scaling Factor	T [GeV]	q	$\langle p_T \rangle$ [GeV/c]	N_0	χ^2/NDF
Figure 1		0–5%	10^5	0.120 ± 0.005	1.093 ± 0.003	0.248 ± 0.013	18,002.8 ± 500	21.146/25
Au–Au		5–10%	10^4	0.120 ± 0.005	1.093 ± 0.003	0.248 ± 0.013	15,202.8 ± 200	21.920/25
200 GeV		10–15%	10^3	0.120 ± 0.005	1.093 ± 0.003	0.248 ± 0.013	12,912.8 ± 150	23.199/25
		15–20%	10^2	0.120 ± 0.005	1.093 ± 0.003	0.248 ± 0.013	10,932.7 ± 150	26.539/25
		20–30%	10	0.120 ± 0.005	1.093 ± 0.003	0.248 ± 0.013	8132.8 ± 140	35.312/25
	π^+	30–40%	1	0.120 ± 0.005	1.093 ± 0.003	0.248 ± 0.013	5842.5 ± 120	83.160/25
		40–50%	10^{-1}	0.120 ± 0.005	1.093 ± 0.003	0.248 ± 0.013	3472.9 ± 100	61.810/25
		50–60%	10^{-2}	0.110 ± 0.004	1.110 ± 0.004	0.232 ± 0.012	2079.8 ± 90	17.099/25
		60–70%	10^{-3}	0.103 ± 0.004	1.118 ± 0.004	0.220 ± 0.012	1160.8 ± 30	9.500/25
		70–80%	10^{-4}	0.093 ± 0.003	1.125 ± 0.005	0.200 ± 0.011	604.9 ± 10	5.473/25
		80–92%	10^{-5}	0.081 ± 0.003	1.135 ± 0.005	0.176 ± 0.009	396.5 ± 5	15.930/25
Figure 1		0–5%	10^5	0.120 ± 0.005	1.093 ± 0.003	0.248 ± 0.013	18,002.8 ± 500	25.491/25
Au–Au		5–10%	10^4	0.120 ± 0.005	1.093 ± 0.003	0.248 ± 0.013	15,202.8 ± 200	27.524/25
200 GeV		10–15%	10^3	0.120 ± 0.005	1.093 ± 0.003	0.248 ± 0.013	12,912.8 ± 150	32.500/25
		15–20%	10^2	0.120 ± 0.005	1.093 ± 0.003	0.248 ± 0.013	10,932.7 ± 150	33.872/25
		20–30%	10	0.120 ± 0.005	1.093 ± 0.003	0.248 ± 0.013	8132.8 ± 140	37.682/25
	π^-	30–40%	1	0.120 ± 0.005	1.093 ± 0.003	0.248 ± 0.013	5642.5 ± 120	77.190/25
		40–50%	10^{-1}	0.120 ± 0.005	1.093 ± 0.003	0.248 ± 0.013	3372.9 ± 100	63.068/25
		50–60%	10^{-2}	0.110 ± 0.004	1.110 ± 0.004	0.232 ± 0.012	2079.8 ± 90	19.137/25
		60–70%	10^{-3}	0.103 ± 0.004	1.118 ± 0.004	0.220 ± 0.012	1160.8 ± 30	10.345/25
		70–80%	10^{-4}	0.093 ± 0.003	1.125 ± 0.005	0.200 ± 0.011	604.9 ± 10	4.824/25
		80–92%	10^{-5}	0.081 ± 0.003	1.135 ± 0.005	0.176 ± 0.009	396.5 ± 5	27.306/25
Figure 1		0–5%	10^5	0.199 ± 0.006	1.060 ± 0.003	0.399 ± 0.020	1880.8 ± 90	40.931/13
Au–Au		5–10%	10^4	0.199 ± 0.006	1.060 ± 0.003	0.399 ± 0.020	1540.7 ± 70	23.196/13
200 GeV		10–15%	10^3	0.199 ± 0.006	1.060 ± 0.003	0.399 ± 0.020	1290.8 ± 50	18.055/13
		15–20%	10^2	0.199 ± 0.006	1.060 ± 0.003	0.399 ± 0.020	1060.8 ± 30	17.045/13
		20–30%	10	0.199 ± 0.006	1.060 ± 0.003	0.399 ± 0.020	779.9 ± 20	21.988/13
	K^+	30–40%	1	0.199 ± 0.006	1.060 ± 0.003	0.399 ± 0.020	495.8 ± 10	30.512/13
		40–50%	10^{-1}	0.199 ± 0.006	1.060 ± 0.003	0.399 ± 0.020	291.5 ± 7	79.333/13
		50–60%	10^{-2}	0.175 ± 0.004	1.070 ± 0.004	0.360 ± 0.018	189.1 ± 7	43.277/13
		60–70%	10^{-3}	0.160 ± 0.004	1.081 ± 0.005	0.337 ± 0.018	98.9 ± 4	69.408/13
		70–80%	10^{-4}	0.155 ± 0.003	1.111 ± 0.006	0.336 ± 0.017	41.9 ± 2	14.914/13
		80–92%	10^{-5}	0.139 ± 0.003	1.122 ± 0.007	0.310 ± 0.016	23.8 ± 1	18.862/13

Table 1. *Cont.*

Collision	Particle	Centrality	Scaling Factor	T [GeV]	q	$\langle p_T \rangle$ [GeV/c]	N_0	χ^2/NDF
Figure 1		0–5%	10^5	0.199 ± 0.006	1.070 ± 0.003	0.402 ± 0.020	1740.7 ± 80	18.282/13
Au–Au		5–10%	10^4	0.199 ± 0.006	1.070 ± 0.003	0.402 ± 0.020	1440.7 ± 50	16.330/13
200 GeV		10–15%	10^3	0.199 ± 0.006	1.070 ± 0.003	0.402 ± 0.020	1180.8 ± 30	16.330/13
		15–20%	10^2	0.199 ± 0.006	1.070 ± 0.003	0.402 ± 0.020	971.6 ± 15	25.125/13
		20–30%	10	0.199 ± 0.006	1.070 ± 0.003	0.402 ± 0.020	719.8 ± 10	27.379/13
	K^-	30–40%	1	0.199 ± 0.006	1.070 ± 0.003	0.402 ± 0.020	453.8 ± 7	71.082/13
		40–50%	10^{-1}	0.199 ± 0.006	1.070 ± 0.003	0.402 ± 0.020	266.6 ± 6	99.387/13
		50–60%	10^{-2}	0.175 ± 0.004	1.080 ± 0.004	0.363 ± 0.018	174.2 ± 4	22.910/13
		60–70%	10^{-3}	0.160 ± 0.004	1.088 ± 0.005	0.339 ± 0.018	89.7 ± 3.7	88.802/13
		70–80%	10^{-4}	0.155 ± 0.003	1.111 ± 0.006	0.336 ± 0.017	40.9 ± 2	14.391/13
		80–92%	10^{-5}	0.139 ± 0.003	1.122 ± 0.007	0.310 ± 0.016	23.1 ± 1	17.794/13
Figure 1		0–5%	10^5	0.291 ± 0.007	1.011 ± 0.003	0.586 ± 0.029	471.8 ± 20	78.267/19
Au–Au		5–10%	10^4	0.291 ± 0.007	1.011 ± 0.003	0.586 ± 0.029	394.8 ± 15	59.704/19
200 GeV		10–15%	10^3	0.291 ± 0.007	1.011 ± 0.003	0.586 ± 0.029	325.9 ± 13	39.207/19
		15–20%	10^2	0.291 ± 0.007	1.011 ± 0.003	0.586 ± 0.029	270.3 ± 10	31.674/19
		20–30%	10	0.291 ± 0.007	1.011 ± 0.003	0.586 ± 0.029	202.2 ± 7	33.076/19
	p	30–40%	1	0.291 ± 0.007	1.011 ± 0.003	0.586 ± 0.029	130.3 ± 5	56.559/19
		40–50%	10^{-1}	0.291 ± 0.007	1.011 ± 0.003	0.586 ± 0.029	76.3 ± 3	137.801/19
		50–60%	10^{-2}	0.240 ± 0.005	1.041 ± 0.003	0.513 ± 0.026	54.3 ± 2	10.924/19
		60–70%	10^{-3}	0.210 ± 0.004	1.071 ± 0.004	0.472 ± 0.024	31.1 ± 1.5	5.877/19
		70–80%	10^{-4}	0.180 ± 0.003	1.089 ± 0.005	0.430 ± 0.022	16.1 ± 0.6	7.078/19
		80–92%	10^{-5}	0.151 ± 0.003	1.105 ± 0.007	0.381 ± 0.019	9.1 ± 0.4	7.293/19
Figure 1		0–5%	10^5	0.291 ± 0.007	1.011 ± 0.003	0.586 ± 0.029	345.8 ± 17	127.757/19
Au–Au		5–10%	10^4	0.291 ± 0.007	1.011 ± 0.003	0.586 ± 0.029	291.8 ± 12	105.070/19
200 GeV		10–15%	10^3	0.291 ± 0.007	1.011 ± 0.003	0.586 ± 0.029	242.8 ± 11	75.153/19
		15–20%	10^2	0.291 ± 0.007	1.011 ± 0.003	0.586 ± 0.029	202.8 ± 10	59.718/19
		20–30%	10	0.291 ± 0.007	1.011 ± 0.003	0.586 ± 0.029	148.3 ± 7	63.202/19
	$\bar{p}$	30–40%	1	0.291 ± 0.007	1.011 ± 0.003	0.586 ± 0.029	96.1 ± 3	69.226/19
		40–50%	10^{-1}	0.291 ± 0.007	1.011 ± 0.003	0.586 ± 0.029	57.0 ± 2	127.930/19
		50–60%	10^{-2}	0.240 ± 0.005	1.041 ± 0.003	0.513 ± 0.026	41.6 ± 1.3	9.229/19
		60–70%	10^{-3}	0.210 ± 0.004	1.071 ± 0.004	0.472 ± 0.024	23.0 ± 1	6.521/19
		70–80%	10^{-4}	0.180 ± 0.003	1.089 ± 0.005	0.430 ± 0.026	11.1 ± 0.4	12.705/19
		80–92%	10^{-5}	0.151 ± 0.003	1.105 ± 0.007	0.381 ± 0.019	7.1 ± 0.2	10.149/17
Figure 1		0–5%	10^2	0.300 ± 0.009	1.009 ± 0.003	0.622 ± 0.031	343.8 ± 15	72.802/14
Au–Au		10–20%	10	0.300 ± 0.009	1.009 ± 0.003	0.622 ± 0.031	261.7 ± 12	8.956/14
200 GeV	Λ	20–40%	1	0.300 ± 0.009	1.009 ± 0.003	0.622 ± 0.031	140.7 ± 7	13.088/14
		40–60%	10^{-1}	0.291 ± 0.008	1.019 ± 0.004	0.611 ± 0.031	53.5 ± 2.3	30.242/14
		60–80%	10^{-2}	0.233 ± 0.006	1.055 ± 0.005	0.522 ± 0.026	23.1 ± 1	20.914/14
Figure 1		0–5%	10^2	0.300 ± 0.009	1.009 ± 0.003	0.622 ± 0.031	330.7 ± 15	11.805/14
Au–Au		10–20%	10	0.300 ± 0.009	1.009 ± 0.003	0.622 ± 0.031	198.6 ± 11	8.060/14
200 GeV	$\bar{\Lambda}$	20–40%	1	0.300 ± 0.009	1.009 ± 0.003	0.622 ± 0.031	110.8 ± 5	8.478/14
		40–60%	10^{-1}	0.291 ± 0.008	1.019 ± 0.004	0.611 ± 0.031	42.5 ± 2	31.308/14
		60–80%	10^{-2}	0.233 ± 0.006	1.055 ± 0.005	0.522 ± 0.026	19.1 ± 0.9	22.080/14
Figure 1		0–5%	10^2	0.317 ± 0.010	1.007 ± 0.003	0.675 ± 0.034	56.4 ± 2.5	6.539/12
Au–Au		10–20%	10	0.317 ± 0.010	1.007 ± 0.003	0.675 ± 0.034	35.1 ± 1.6	14.221/12
200 GeV	Ξ^-	20–40%	1	0.317 ± 0.010	1.007 ± 0.004	0.675 ± 0.034	17.6 ± 0.6	6.523/12
		40–60%	10^{-1}	0.310 ± 0.009	1.009 ± 0.005	0.665 ± 0.033	6.6 ± 0.3	14.694/11
		60–80%	10^{-2}	0.288 ± 0.008	1.039 ± 0.006	0.637 ± 0.032	1.7 ± 0.06	1.126/4
Figure 1		0–5%	10^2	0.317 ± 0.010	1.007 ± 0.003	0.675 ± 0.034	48.5 ± 2	5.077/12
Au–Au		10–20%	10	0.317 ± 0.010	1.007 ± 0.003	0.675 ± 0.034	28.6 ± 1.3	6.937/12
200 GeV	$\bar{\Xi}^+$	20–40%	1	0.317 ± 0.010	1.007 ± 0.003	0.675 ± 0.034	15.2 ± 0.4	12.527/12
		40–60%	10^{-1}	0.310 ± 0.009	1.009 ± 0.004	0.665 ± 0.033	5.7 ± 0.2	7.698/11
		60–80%	10^{-2}	0.288 ± 0.008	1.039 ± 0.005	0.637 ± 0.032	1.6 ± 0.04	7.577/4

Table 1. *Cont.*

Collision	Particle	Centrality	Scaling Factor	T [GeV]	q	$\langle p_T \rangle$ [GeV/c]	N_0	χ^2/NDF
Figure 1		0–5%	10	0.340 ± 0.011	1.005 ± 0.003	0.756 ± 0.038	11.4 ± 0.3	8.195/2
Au–Au	$\Omega^- + \bar{\Omega}^+$	20–40%	1	0.340 ± 0.011	1.005 ± 0.003	0.756 ± 0.038	3.6 ± 1	1.038/2
200 GeV		40–60%	10^{-1}	0.326 ± 0.010	1.020 ± 0.004	0.740 ± 0.037	1.2 ± 0.02	4.844/2
Figure 2		0–5%	10^5	0.139 ± 0.006	1.112 ± 0.003	0.299 ± 0.015	35,532.8 ± 1600	92.407/38
Pb–Pb		5–10%	10^4	0.139 ± 0.006	1.112 ± 0.003	0.299 ± 0.015	29,152.6 ± 1000	98.374/38
2.76 TeV		10–20%	10^3	0.139 ± 0.006	1.112 ± 0.003	0.299 ± 0.015	21,852.5 ± 900	109.029/38
		20–30%	10^2	0.139 ± 0.006	1.112 ± 0.003	0.299 ± 0.015	14,662.4 ± 700	130.250/38
		30–40%	10	0.139 ± 0.006	1.112 ± 0.003	0.299 ± 0.015	9302.4 ± 450	150.174/38
	π^+	40–50%	1	0.139 ± 0.006	1.112 ± 0.003	0.299 ± 0.015	5612.4 ± 250	177.151/38
		50–60%	10^{-1}	0.122 ± 0.004	1.133 ± 0.004	0.272 ± 0.014	3692.4 ± 150	110.983/38
		60–70%	10^{-2}	0.117 ± 0.003	1.137 ± 0.005	0.261 ± 0.013	2012.4 ± 100	110.343/38
		70–80%	10^{-3}	0.109 ± 0.003	1.146 ± 0.006	0.246 ± 0.012	1004.3 ± 50	88.114/38
		80–90%	10^{-4}	0.099 ± 0.002	1.152 ± 0.007	0.225 ± 0.011	454.3 ± 22	50.313/38
Figure 2		0–5%	10^5	0.139 ± 0.006	1.112 ± 0.003	0.299 ± 0.015	35,422.7 ± 1600	88.847/38
Pb–Pb		5–10%	10^4	0.139 ± 0.006	1.112 ± 0.003	0.299 ± 0.015	29,151.3 ± 1000	88.816/38
2.76 TeV		10–20%	10^3	0.139 ± 0.006	1.112 ± 0.003	0.299 ± 0.015	21,850.2 ± 900	100.893/38
		20–30%	10^2	0.139 ± 0.006	1.112 ± 0.003	0.299 ± 0.015	14,660.1 ± 700	117.337/38
		30–40%	10	0.139 ± 0.006	1.112 ± 0.003	0.299 ± 0.015	9300.3 ± 450	139.216/38
	π^-	40–50%	1	0.139 ± 0.006	1.112 ± 0.003	0.299 ± 0.015	5610.1 ± 250	169.678/38
		50–60%	10^{-1}	0.122 ± 0.004	1.133 ± 0.004	0.272 ± 0.014	3690.3 ± 150	97.970/38
		60–70%	10^{-2}	0.117 ± 0.003	1.137 ± 0.005	0.261 ± 0.013	2012.1 ± 100	96.553/38
		70–80%	10^{-3}	0.109 ± 0.003	1.146 ± 0.006	0.246 ± 0.012	1004.3 ± 50	79.539/38
		80–90%	10^{-4}	0.099 ± 0.002	1.152 ± 0.007	0.225 ± 0.011	454.3 ± 22	44.653/38
Figure 2		0–5%	10^5	0.243 ± 0.007	1.075 ± 0.004	0.485 ± 0.024	3630.7 ± 150	21.814/33
Pb–Pb		5–10%	10^4	0.243 ± 0.007	1.075 ± 0.004	0.485 ± 0.024	3000.6 ± 140	15.458/33
2.76 TeV		10–20%	10^3	0.243 ± 0.007	1.075 ± 0.004	0.485 ± 0.024	2250.3 ± 100	10.306/33
		20–30%	10^2	0.243 ± 0.007	1.075 ± 0.004	0.485 ± 0.024	1500.5 ± 70	5.780/33
		30–40%	10	0.243 ± 0.007	1.075 ± 0.004	0.485 ± 0.024	964.5 ± 40	9.591/33
	K^+	40–50%	1	0.243 ± 0.007	1.075 ± 0.004	0.485 ± 0.024	578.5 ± 25	34.837/33
		50–60%	10^{-1}	0.224 ± 0.006	1.081 ± 0.005	0.453 ± 0.023	347.6 ± 15	13.505/33
		60–70%	10^{-2}	0.209 ± 0.005	1.095 ± 0.007	0.431 ± 0.022	185.4 ± 7	14.853/33
		70–80%	10^{-3}	0.197 ± 0.004	1.101 ± 0.007	0.411 ± 0.021	85.3 ± 3	19.568/33
		80–90%	10^{-4}	0.180 ± 0.003	1.115 ± 0.008	0.384 ± 0.019	35.3 ± 1.4	24.426/33
Figure 2		0–5%	10^5	0.243 ± 0.007	1.075 ± 0.004	0.485 ± 0.024	3611.8 ± 150	13.938/33
Pb–Pb		5–10%	10^4	0.243 ± 0.007	1.075 ± 0.004	0.485 ± 0.024	3000.6 ± 140	12.678/33
2.76 TeV		10–20%	10^3	0.243 ± 0.007	1.075 ± 0.004	0.485 ± 0.024	2250.3 ± 100	9.671/33
		20–30%	10^2	0.243 ± 0.007	1.075 ± 0.004	0.485 ± 0.024	1500.5 ± 70	5.821/33
		30–40%	10	0.243 ± 0.007	1.075 ± 0.004	0.485 ± 0.024	964.5 ± 40	15.710/33
	K^-	40–50%	1	0.243 ± 0.007	1.075 ± 0.004	0.485 ± 0.024	578.5 ± 25	42.682/33
		50–60%	10^{-1}	0.224 ± 0.006	1.081 ± 0.005	0.453 ± 0.023	347.6 ± 15	25.433/33
		60–70%	10^{-2}	0.209 ± 0.005	1.095 ± 0.007	0.431 ± 0.022	185.4 ± 7	18.010/33
		70–80%	10^{-3}	0.197 ± 0.004	1.101 ± 0.007	0.411 ± 0.021	85.3 ± 3	22.596/33
		80–90%	10^{-4}	0.180 ± 0.003	1.115 ± 0.008	0.384 ± 0.019	35.3 ± 1.4	30.885/33
Figure 2		0–5%	10^5	0.370 ± 0.008	1.033 ± 0.003	0.724 ± 0.039	733.8 ± 31	60.283/39
Pb–Pb		5–10%	10^4	0.370 ± 0.008	1.033 ± 0.003	0.724 ± 0.039	612.7 ± 25	53.695/39
2.76 TeV		10–20%	10^3	0.370 ± 0.008	1.033 ± 0.003	0.724 ± 0.039	464.7 ± 20	42.885/39
		20–30%	10^2	0.370 ± 0.008	1.033 ± 0.003	0.724 ± 0.039	321.5 ± 13	45.930/39
		30–40%	10	0.370 ± 0.008	1.033 ± 0.003	0.724 ± 0.039	209.3 ± 7	69.347/39
	p	40–50%	1	0.370 ± 0.008	1.033 ± 0.003	0.724 ± 0.039	119.1 ± 5	130.548/39
		50–60%	10^{-1}	0.330 ± 0.007	1.038 ± 0.004	0.660 ± 0.034	85.9 ± 3	81.913/39
		60–70%	10^{-2}	0.305 ± 0.006	1.044 ± 0.004	0.621 ± 0.031	47.8 ± 1.7	21.809/39
		70–80%	10^{-3}	0.269 ± 0.005	1.068 ± 0.005	0.572 ± 0.029	24.9 ± 1.2	20.626/39
		80–90%	10^{-4}	0.230 ± 0.003	1.079 ± 0.005	0.509 ± 0.025	11.5 ± 0.5	25.275/39

Table 1. *Cont.*

Collision	Particle	Centrality	Scaling Factor	T [GeV]	q	$\langle p_T \rangle$ [GeV/c]	N_0	χ^2/NDF
Figure 2		0–5%	10^5	0.370 ± 0.008	1.033 ± 0.003	0.724 ± 0.039	733.7 ± 30	48.747/39
Pb–Pb		5–10%	10^4	0.370 ± 0.008	1.033 ± 0.003	0.724 ± 0.039	612.7 ± 25	45.637/39
2.76 TeV		10–20%	10^3	0.370 ± 0.008	1.033 ± 0.003	0.724 ± 0.039	464.7 ± 20	35.998/39
		20–30%	10^2	0.370 ± 0.008	1.033 ± 0.003	0.724 ± 0.039	321.5 ± 13	41.931/39
		30–40%	10	0.370 ± 0.008	1.033 ± 0.003	0.724 ± 0.039	209.3 ± 7	82.599/39
	$\bar{p}$	40–50%	1	0.370 ± 0.008	1.033 ± 0.003	0.724 ± 0.039	119.1 ± 5	140.624/39
		50–60%	10^{-1}	0.330 ± 0.007	1.038 ± 0.004	0.660 ± 0.034	85.9 ± 3	22.102/39
		60–70%	10^{-2}	0.305 ± 0.006	1.044 ± 0.004	0.621 ± 0.031	47.8 ± 1	27.317/39
		70–80%	10^{-3}	0.269 ± 0.005	1.068 ± 0.005	0.572 ± 0.029	24.9 ± 1.2	17.769/39
		80–90%	10^{-4}	0.230 ± 0.003	1.079 ± 0.005	0.509 ± 0.025	11.4 ± 0.5	29.115/39
Figure 2		0–5%	10^3	0.400 ± 0.009	1.012 ± 0.003	0.781 ± 0.040	552.8 ± 25	104.160/23
Pb–Pb		5–10%	10^2	0.400 ± 0.009	1.012 ± 0.003	0.781 ± 0.040	4711.8 ± 20	84.937/23
2.76 TeV	Λ	10–20%	10	0.400 ± 0.009	1.012 ± 0.003	0.781 ± 0.040	363.9 ± 15	56.286/23
		20–40%	1	0.400 ± 0.009	1.012 ± 0.003	0.781 ± 0.040	199.8 ± 7	32.299/23
		40–60%	4×10^{-1}	0.380 ± 0.008	1.011 ± 0.004	0.749 ± 0.037	80.8 ± 3	20.298/23
		60–80%	9×10^{-2}	0.320 ± 0.007	1.047 ± 0.005	0.668 ± 0.033	23.1 ± 1.2	8.916/23
		80–90%	25×10^{-3}	0.278 ± 0.006	1.067 ± 0.005	0.606 ± 0.030	5.1 ± 0.23	14.769/23
Figure 2		0–10%	10^2	0.425 ± 0.010	1.003 ± 0.003	0.843 ± 0.042	70.2 ± 2	98.477/19
Pb–Pb		10–20%	10	0.425 ± 0.010	1.003 ± 0.003	0.843 ± 0.042	50.7 ± 2	49.606/19
2.76 TeV	Ξ^-	20–40%	1	0.425 ± 0.010	1.003 ± 0.003	0.843 ± 0.042	27.1 ± 1.2	25.780/19
		40–60%	3×10^{-1}	0.410 ± 0.009	1.005 ± 0.002	0.820 ± 0.041	9.8.0 ± 0.5	20.924/19
		60–80%	7×10^{-2}	0.363 ± 0.007	1.022 ± 0.002	0.754 ± 0.038	2.6 ± 0.2	15.382/16
Figure 2		0–10%	10^2	0.425 ± 0.010	1.003 ± 0.003	0.843 ± 0.042	67.3 ± 2	83.259/19
Pb–Pb		10–20%	10	0.425 ± 0.010	1.003 ± 0.003	0.843 ± 0.042	48.6 ± 2	40.399/19
2.76 TeV	$\bar{\Xi}^+$	20–40%	1	0.425 ± 0.010	1.003 ± 0.003	0.843 ± 0.042	27.1 ± 1.2	36.604/19
		40–60%	3×10^{-1}	0.410 ± 0.009	1.005 ± 0.002	0.820 ± 0.041	9.8 ± 0.5	21.082/19
		60–80%	7×10^{-2}	0.363 ± 0.007	1.022 ± 0.002	0.754 ± 0.038	2.4 ± 0.2	21.887/16
Figure 2		0–10%	10^2	0.474 ± 0.011	1.002 ± 0.003	0.964 ± 0.048	10.2 ± 0.5	10.323/10
Pb–Pb		10–20%	10	0.474 ± 0.011	1.002 ± 0.003	0.964 ± 0.048	6.9 ± 0.25	8.439/10
2.76 TeV	Ω^-	20–40%	1	0.474 ± 0.011	1.002 ± 0.003	0.964 ± 0.048	3.6 ± 0.15	11.302/10
		40–60%	3×10^{-1}	0.439 ± 0.010	1.004 ± 0.002	0.911 ± 0.046	1.4 ± 0.06	15.954/9
		60–80%	17×10^{-2}	0.420 ± 0.009	1.019 ± 0.002	0.888 ± 0.044	0.22 ± 0.01	6.524/7
Figure 2		0–10%	10^2	0.474 ± 0.011	1.002 ± 0.003	0.964 ± 0.048	10.2 ± 0.5	10.661/10
Pb–Pb		10–20%	10	0.474 ± 0.011	1.002 ± 0.003	0.964 ± 0.048	7.5 ± 0.25	20.167/10
2.76 TeV	$\bar{\Omega}^+$	20–40%	1	0.474 ± 0.011	1.002 ± 0.003	0.964 ± 0.048	3.6 ± 0.15	8.580/10
		40–60%	3×10^{-1}	0.439 ± 0.010	1.004 ± 0.002	0.911 ± 0.046	1.3 ± 0.06	14.629/9
		60–80%	17×10^{-2}	0.420 ± 0.009	1.019 ± 0.002	0.888 ± 0.044	0.22 ± 0.01	8.081/7
Figure 3	π^+	-	10^5	0.083 ± 0.003	1.126 ± 0.005	0.178 ± 0.009	144.5 ± 5	78.052/20
p–p	π^-	-	10^4	0.083 ± 0.003	1.126 ± 0.005	0.178 ± 0.009	144.5 ± 5	75.958/20
200 GeV	K_s^0	-	10^3	0.144 ± 0.007	1.112 ± 0.007	0.317 ± 0.016	7.1 ± 0.25	41.866/19
	p	-	10^2	0.148 ± 0.002	1.110 ± 0.007	0.376 ± 0.019	4.0 ± 0.15	43.374/17
	$\bar{p}$	-	10	0.148 ± 0.004	1.110 ± 0.007	0.376 ± 0.019	4.0 ± 0.15	12.662/17
	Λ	-	1	0.225 ± 0.005	1.033 ± 0.006	0.509 ± 0.026	1.2 ± 0.05	72.374/18
	$\bar{\Lambda}$	-	10^{-1}	0.225 ± 0.005	1.033 ± 0.006	0.509 ± 0.026	1.1 ± 0.04	107.538/18
	Ξ^-	-	10^{-1}	0.288 ± 0.008	1.029 ± 0.004	0.637 ± 0.032	0.04 ± 0.002	13.664/8
	$\bar{\Xi}^+$	-	10^{-2}	0.288 ± 0.008	1.029 ± 0.004	0.637 ± 0.032	0.04 ± 0.002	22.374/8
	$\Omega^- + \bar{\Omega}^+$	-	0.3×10^{-2}	0.326 ± 0.010	1.020 ± 0.003	0.737 ± 0.037	0.0055 ± 0.0003	0.487/0
Figure 3	π^+	-	10^3	0.099 ± 0.003	1.152 ± 0.007	0.224 ± 0.011	162.2 ± 7	68.700/19
p–p	π^-	-	10^2	0.099 ± 0.003	1.152 ± 0.007	0.223 ± 0.011	160.2 ± 7	56.251/19
2.76 TeV	K^+	-	10	0.176 ± 0.004	1.115 ± 0.008	0.377 ± 0.019	12.6 ± 0.6	11.354/14
	K^-	-	1	0.176 ± 0.004	1.115 ± 0.008	0.377 ± 0.019	12.4 ± 0.5	13.413/14
	p	-	2×10^{-1}	0.223 ± 0.005	1.079 ± 0.005	0.497 ± 0.025	4.2 ± 0.15	64.225/24
	$\bar{p}$	-	2×10^{-2}	0.223 ± 0.006	1.079 ± 0.005	0.497 ± 0.025	4.1 ± 0.15	46.396/24

Trends of Parameters

Figure 4 demonstrates the fluctuating behaviour of the parameters with centrality, mass and size of the system. Different symbols are used in order to differentiate particles. The behaviour of the parameters in panels (a)–(h) with changing centrality is indicated by the trend of symbols from left to right, while panels (i)–(l) show the mass dependence of the relevant parameters. Panels (a), (b), (c) and (d) present the behaviour of the relative parameters obtained from Au–Au collisions at 200 GeV, while the parameters obtained from Pb–Pb collisions are presented in panels (e), (f), (g) and (h). Panels (i), (j), (k) and (l) show the dependence of the relevant parameters on particle species in pp collisions at 200 GeV and 2.76 TeV. In panels (i) to (l), the red-coloured symbols denote 200 GeV while green symbols denote 2.76 TeV.

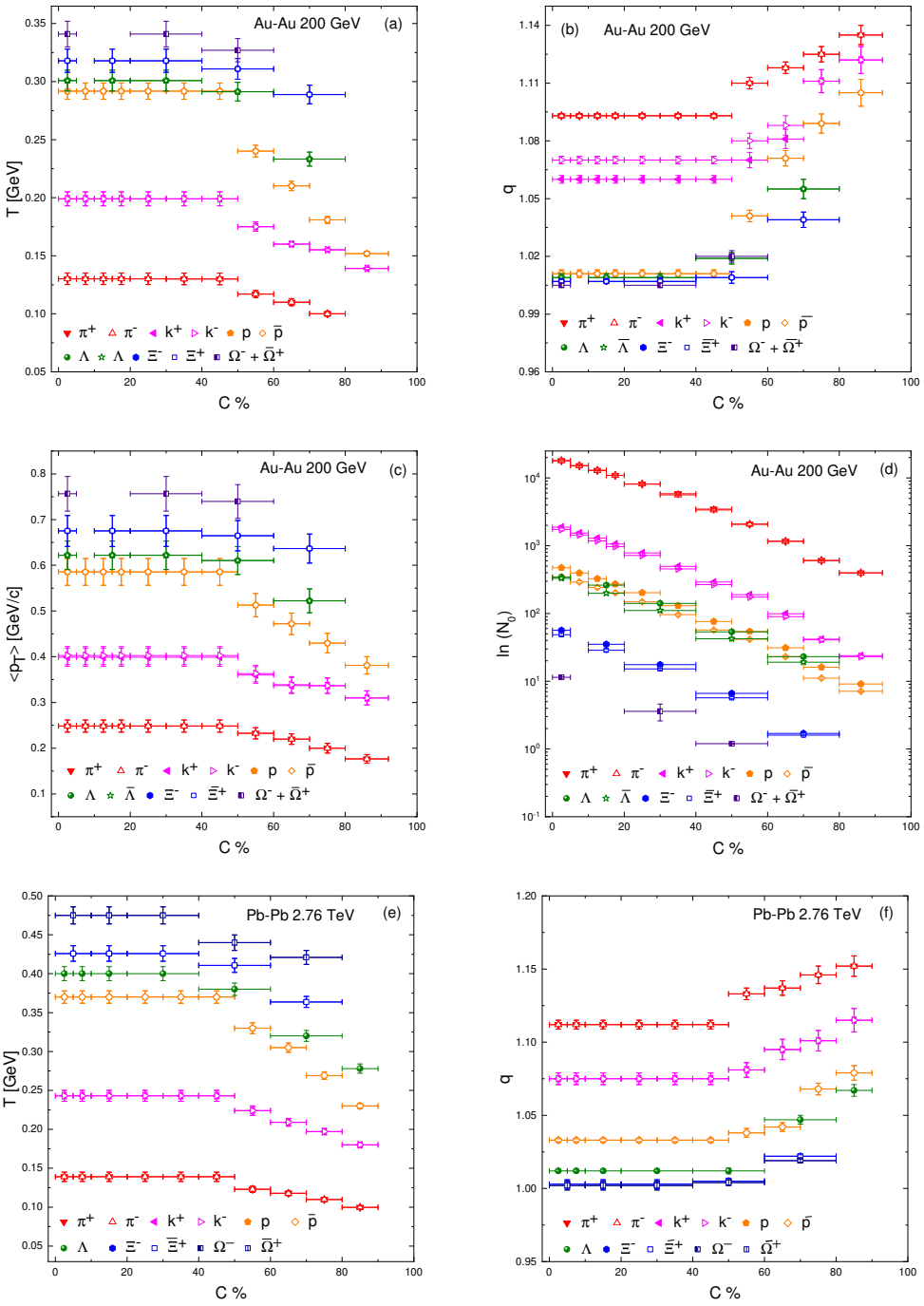

Figure 4. *Cont.*

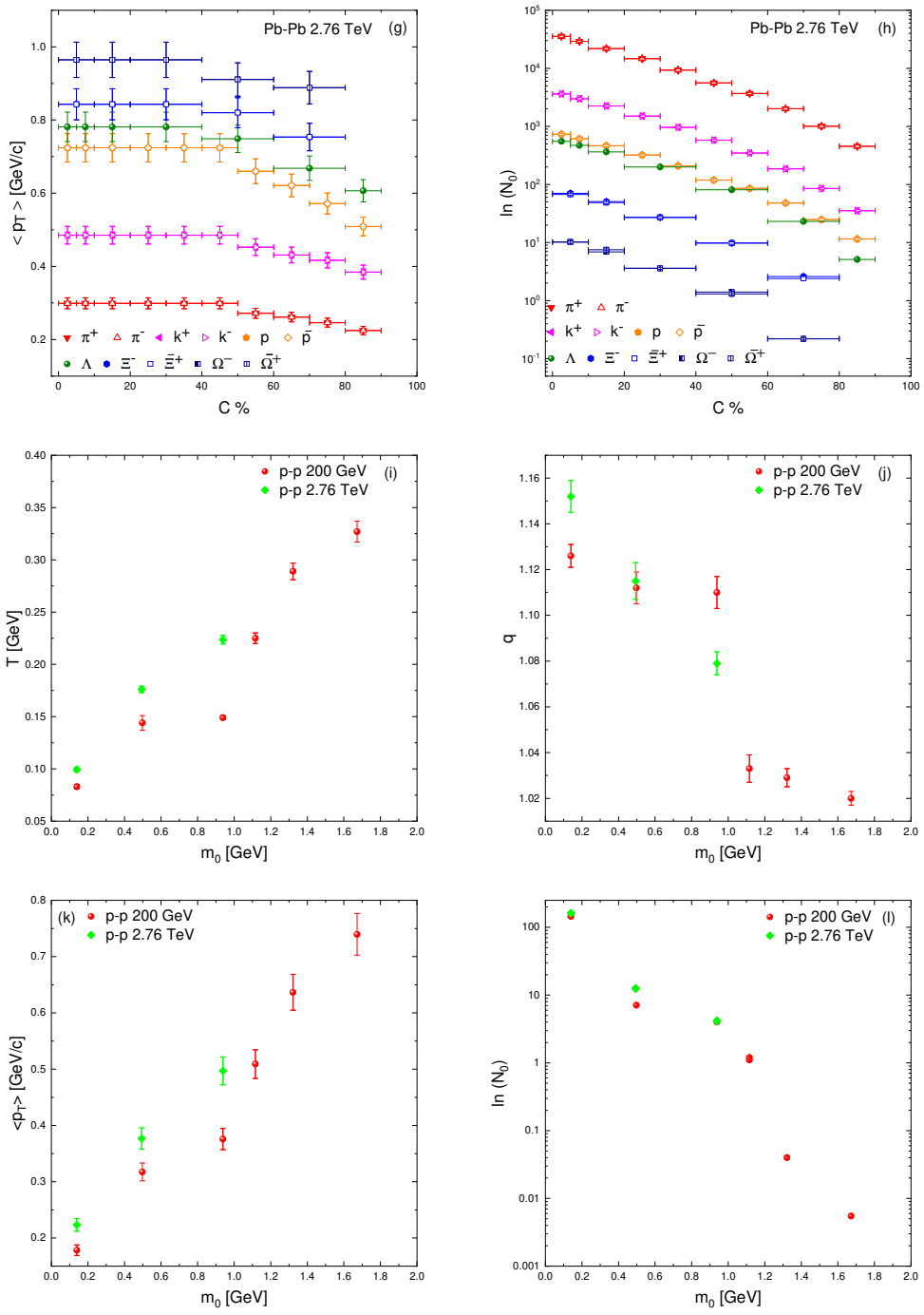

Figure 4. Plots (**a**–**d**) show the dependence of T, q, $\langle p_T \rangle$ and N_0 on centrality (C%), respectively, in Au–Au collision at $\sqrt{s_{NN}}$ = 200 GeV, while plots (**e**–**h**) represent the dependence of the same parameters on C%, respectively, in Pb–Pb collision at $\sqrt{s_{NN}}$ = 2.76 TeV. Plots (**i**–**l**) present the dependence of the said parameters on the rest masses of the produced particles, respectively, in p–p collision at $\sqrt{s}$ = 200 GeV and $\sqrt{s}$ = 2.76 TeV.

We reported that the effective temperature T increases from peripheral to central collisions as shown in Figure 4a,e, which specifies the non-violent reaction having happened in the peripheral collisions that becomes intense as the system heads on towards more central events. Due to the large number of participant nucleons, the intense reaction in the central collisions leads the system to obtain a higher degree of excitation as a large amount of energy is deposited per nucleon in the system. We note that overall, T increases

from peripheral to central collisions, but a smooth behaviour is seen from 40 to 50% to the most central collisions. This smooth behaviour is due to the fact that as the system experiences more central collisions, it becomes more and more thermalized. T reaches its maximum value at 40% or 50% centrality, and more collision energy is deposited in a larger volume rather than higher temperature. The two observed regions correspond to different mechanisms according to our belief. The region from 0 to 40% centrality is a meson-dominated region where QGP is produced, while the region beyond this is baryon-dominated, to the most periphery. As a large amount of energy is deposited in the meson-dominated region, phase transition possibly occurs in this region, while the baryon-dominated region absorbs less energy and hence it is difficult for the hot and dense medium to be formed in this region. Such effect of meson domination is observed in Refs. [50,51]. It is very important to notice that similar studies are present in the literature [51,52], but the present work is different from them in several aspects. Firstly, we need different functions to analyze the data because different functions and models may have different results [32,53,54], and our present work has used a different function from [55]. Secondly, we have studied the dependence of temperature on centrality, and our result shows saturation of temperature in the central collisions which is not the case in other sources in the literature to our knowledge. Furthermore, the present work reported a mass differential freeze-out scenario. Massive particles are left behind in the system due to large inertia because of their mass (but not due to large thermal or flow motion), therefore, they freeze-out earlier than the lighter particles. It should be noted that we have performed the individual fit which results in multiple kinetic freeze-out scenarios. One can also perform the simultaneous fit and can obtain a single freeze-out scenario. In fact, the freeze-out of the particles is a complex scenario and is an open question in the community. We have used the individual fit due to the reason that a large number of particles are involved in the collisions with different properties and production mechanisms. In simultaneous fitting, all the particle spectra are fitted simultaneously, which can be challenging due to the complexity of the system. It becomes difficult to account for all possible interactions and dynamics that affect different particle species. While the individual fitting to each particle allows a more focused analysis of each particle species, taking into account their specific production mechanisms and interactions.

Figure 4b,f demonstrate the centrality-dependent q. q is an entropy-based parameter which is used to measure of non-equilibriation of the system. We observed although from the most central to 40–50%, q remains constant but overall q increases from central to peripheral collisions. If q is closer to unity, it specifies the system to be closer to equilibrium. In the present work, q in central collisions is closer to unity, therefore they approach the full equilibrium quickly. T and q are directly related to the freeze-out conditions. We can see that T is larger while q is more closer to unity which gives strength to the idea of quick equilibriation of the central collision systems. Similarly, for heavier particles T is larger while q is smaller, this strengthens the claim of the early freeze-out of the massive particles. $\langle p_T \rangle$ as a function of centrality is shown in Figure 4c,g, and it follows the same trend as T. In fact, a central collision system transfers large momentum and then further multiple scattering happens. In this work, T is the reflection of $\langle p_T \rangle$. We also observed that the values of T, $\langle p_T \rangle$ and q in p–p collisions are approximately equal to that in peripheral A–A collisions at the same centre of mass energies. This indicates that the thermodynamic nature of A–A peripheral collisions is similar to that of p–p collisions. This result is in agreement with our previous results [56].

N_0 is shown to be increasing from peripheral to central collisions in Figure 4d,h. Although N_0 is the parameter of normalization, it expresses particle multiplicity. Indeed, the central reaction consists of a large number of participants, which corresponds to a harsh reaction, and correspondingly results in large multiplicity. N_0 is also dependent on particle species. The more massive the particle, the less the multiplicity. Moreover, one can clearly see from Table 1 that the multiplicity parameter for a particle and its antiparticle is the same, which means that both are produced in equal amounts or produced symmetrically.

Figure 4i–l demonstrate the dependence of the parameters on particle species in p–p collisions. These parameters are dependent on particle species as they are in Au–Au and Pb–Pb collisions. Larger T and $\langle p_T \rangle$ and smaller q and N_0 for the heavier particles are observed in p–p collisions. T and $\langle p_T \rangle$ are obviously seen to be larger at LHC than RHIC, showing their energy dependence.

From the above results, we also reported that T, $\langle p_T \rangle$ and N_0 are dependent on the size of the colliding system. The larger the collision system, the larger these parameters are. As larger collision systems have participants involved in the interaction, it experiences an intense reaction, where more energy is deposited in the system, which corresponds to a large transfer of momentum that naturally leads the system to be highly excited. Furthermore, due to the large transfer of energy (momentum), further multiple scattering happens and that results in a larger N_0 (multiplicity). We have seen that pions are almost identical in Au–Au and Pb–Pb collisions. We believe that the pions are abundant hadrons produced in a collision and their production mechanisms are well-established. The larger number of pions provide a statistically significant measurement, allowing for a precise determination of their freeze-out temperature. The dominance of pions in the hadron spectra can outweigh the contributions of other particles, which result in a consistent freeze-out temperature for pions across different collision systems.

To see the correlations among different parameters, we combine different panels of Figure 4 in Figure 5. Figure 5a shows the correlation of T and $\langle p_T \rangle$, while Figure 5b–e show the correlation of T and q, q and $\langle p_T \rangle$, T and N_0, and $\langle p_T \rangle$ and N_0. The correlation of T and $\langle p_T \rangle$ can be explained by noting that large participants in the central reaction result in a very large energy (momentum) transfer in the system that corresponds to a higher degree of excitation of the respective system. Similarly, larger T in the central system refers to the early freeze-out of the system, while smaller q suggests the system quickly reaches equilibrium. In fact, larger T and small q are obtained in central collisions, while smaller T and larger q are in peripheral collisions. This is consistent with [57] where the authors presented a positive correlation among T and n where they used the Tsallis distribution for Maxwell–Boltzmann particles. $n = 1/(q-1)$, since the present work specifies a negative correlation of T and q, therefore they are concordant. This result also agrees with another work [58]. The correlation between T and q is observed to be considerable. Meanwhile, the correlation of q and $\langle p_T \rangle$ in Figure 5c gives strength to the result of the correlation of T and q because T is the reflection of $\langle p_T \rangle$. It means that $T \propto \langle p_T \rangle \propto 1/q$. Panel (d) and (e) present the correlation of T and N_0 and $\langle p_T \rangle$ and N_0. They have a positive correlation. Larger T corresponds to larger N_0. This can be explained observing that the central collision system consists of a large number of participants to be involved in the interaction, which naturally results in the production of a large number of multiple scatterings, and the degree of excitation of the system is larger in central collisions due to the harsh collision reaction where more energy is deposited in the system and ultimately result in larger $\langle p_T \rangle$. This shows that $T \propto \langle p_T \rangle \propto N_0$. It should be noted that $\langle p_T \rangle$ basically provides information about the collective motion and flow of the particles in the system. The relation between T and $\langle p_T \rangle$ arises from the interplay between the collective motion and temperature during the freeze-out process. As the system expands, the collective motion of the particles can attribute to the transverse momentum, and this collective motion is influenced by the temperature of the system. In the present work, we observed T to be proportional to approximately 2*$\langle p_T \rangle$ which may indicate a balance between thermal motion and collective flow. The factor 2 can arise due to specific dynamics of the system and statistical behaviour of the particles. We also noted that T is independent of the particle multiplicity as the later observable does not remain constant in the central collisions. The behaviour of multiplicity with T can depend on several factors such as the collision system, collision energy regime, and analysis techniques. Different theoretical models and experimental observables may also lead to variations in the observed behaviors. Studying the interplay between various physical processes and their effects on T and particle multiplicity provides valuable insights into the dynamics of heavy ion collisions, and the properties of the created

system. In deed, more studies are needed to fully understand the relationship between T and particle multiplicity.

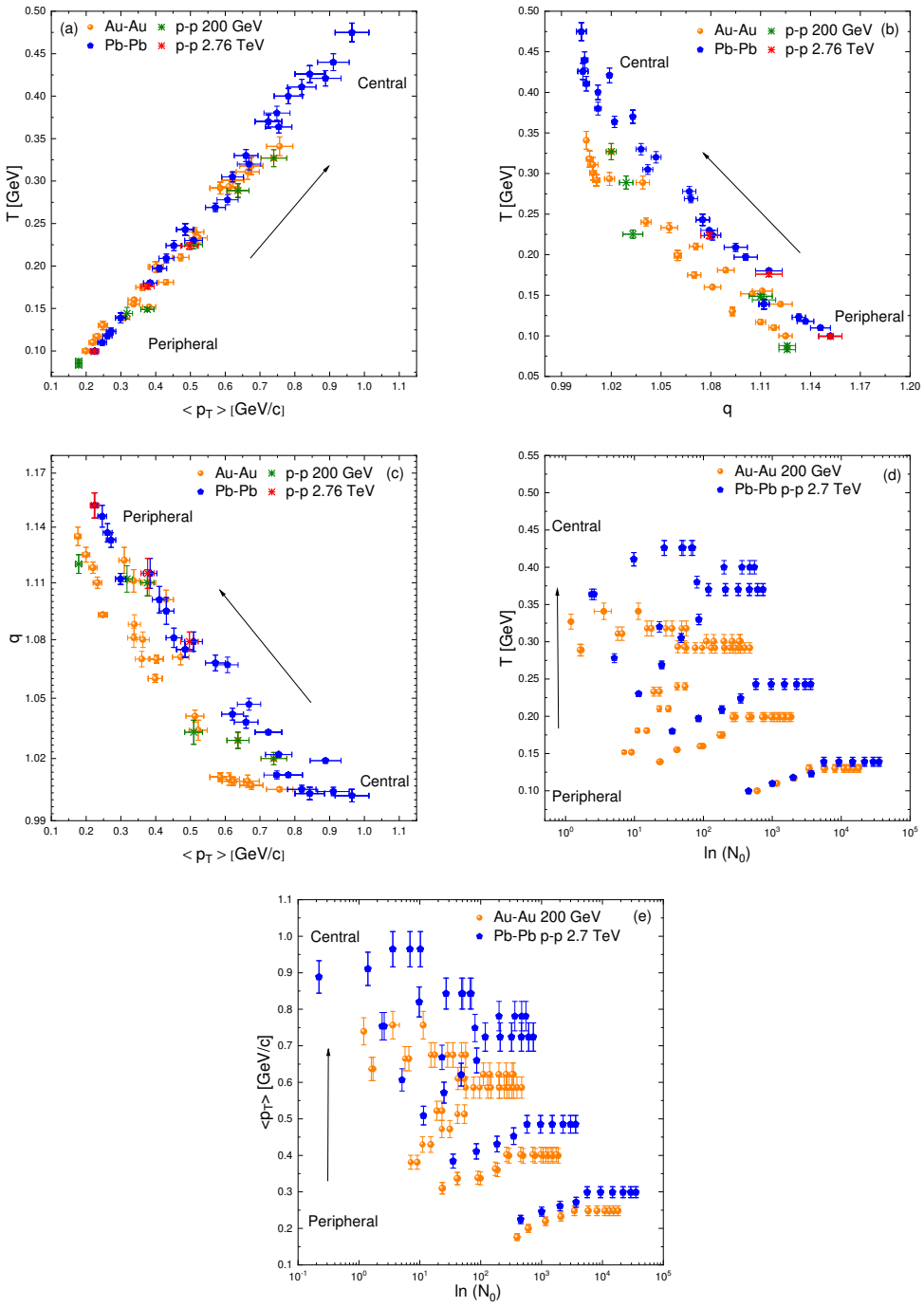

Figure 5. Plots (**a**–**e**) show the correlation of T and $\langle p_T \rangle$, T and q, q and $\langle p_T \rangle$, T and $ln(N_0)$, and $\langle p_T \rangle$ and $ln(N_0)$, respectively, in different centrality bins in Au–Au collision at $\sqrt{s_{NN}}$ = 200 GeV and in Pb–Pb collision at $\sqrt{s_{NN}}$ = 2.76 TeV, plots (**a**–**c**) also show the results from p–p collision at these collision energies which are comparable to the results of peripheral A–A collision at the same energy.

As mentioned earlier, T depends on the kinetic freeze-out temperature and flow velocity; we can extract both these parameters from T if the centrality interval for all of them is the same. In the present work, the centralities of all the particles are not the same and it is difficult to make them the same and is in fact beyond the focus of the present work. But to show the extraction of the kinetic freeze-out temperature T_0 and transverse flow velocity β_T from T, we took the particles with the same centrality and extracted the

two parameters from it. We can see that the centrality intervals of the light particles are the same, so we took the light particles and performed the linear fitting among T and m_0 by $x = am_0 + b$ in Figure 6a,b for Au–Au and Pb–Pb collisions, respectively. The slopes and intercepts along with the value of χ^2 are extracted and are labelled in Table 2 where a is the slope and b is the intercept, and the intercepts in Figure 6a,b are regarded as the kinetic freeze-out temperature [57,59–61]. For the extraction of transverse flow velocity, we performed the linear fit among $\langle p_T \rangle$ and mean moving mass ($\bar{m}$). The intercepts, slopes and values of χ^2 are presented in Table 3. The slope is regarded as the transverse flow velocity (β_T) [62]. Figure 7a,b represent the average kinetic freeze-out temperature and average transverse flow velocity of the particles obtained through the linear fitting as a function of the collision centrality. The green symbols show the result for Au–Au collisions, while the red symbols are used to represent the results of Pb–Pb collisions. One can see that the trend of T_0 and β_T with centrality is similar to that of T which evinces that the excitation function of T, and T_0 as well as β_T are similar. We noticed that the parameters from the most central collisions to 0–50% centrality classes are the same with same uncertainties but have different data/fit ratios and different values of χ^2. The same values of the parameters in these centrality bins suggest that the system has reached a similar degree of thermalization across these centrality intervals. This can be due to the fact that the collision dynamics and resulting particle production processes are similar in these centrality intervals. However the data/fit ratios and the values of χ^2 changes due to statistical fluctuation. Both the experimental data and theoretical models are subjected to statistical uncertainties, which can lead to variations in the data/fit ratio and values of χ^2.

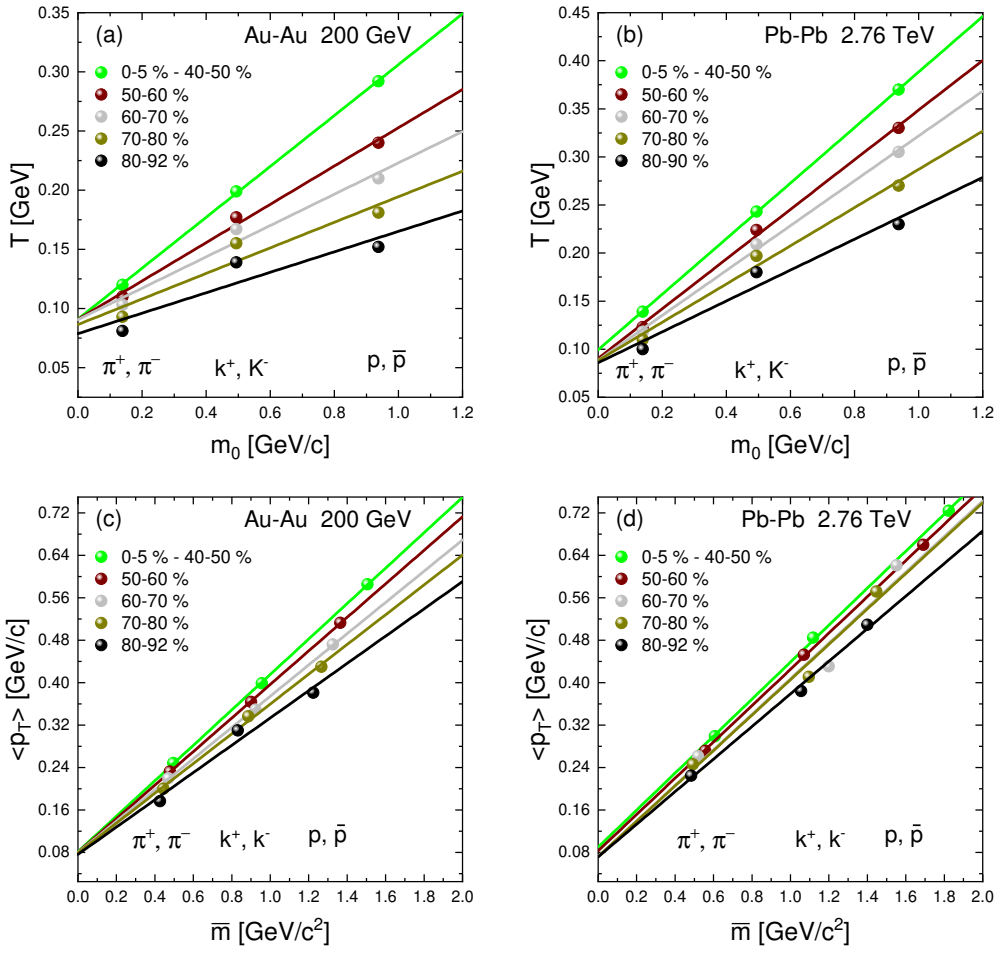

Figure 6. Dependence of T and m_0 in panels (**a**), (**b**) and $\langle p_T \rangle$ and $\bar{m}$ in panels (**c**) and (**d**), respectively. The curve over the data points is the fit by linear equation.

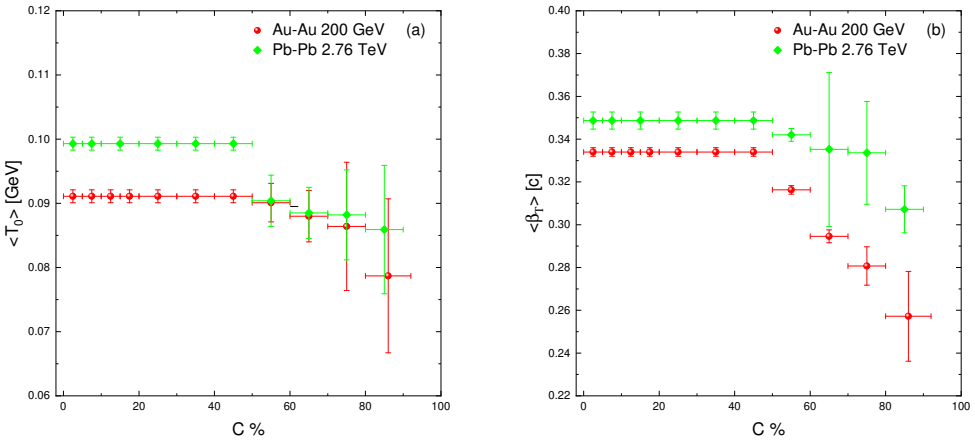

Figure 7. Dependence of (**a**) $\langle T_0 \rangle$ and (**b**) $\langle \beta_T \rangle$ on centrality in Au–Au and Pb–Pb collisions, respectively.

Table 2. Values of intercepts, slopes and χ^2 obtained from the linear fitting of T vs. m_0 plot.

Collision	Centrality	Intercept	Slope	χ^2
Au–Au 200 GeV	0–5%	0.0911 ± 0.001	0.2150 ± 0.002	0.0015
	5–10%	0.0911 ± 0.001	0.2150 ± 0.002	0.0015
	10–15%	0.0911 ± 0.001	0.2150 ± 0.002	0.0015
	15–20%	0.0911 ± 0.001	0.2150 ± 0.002	0.0015
	20–30%	0.0911 ± 0.001	0.2150 ± 0.002	0.0015
	30–40%	0.0911 ± 0.001	0.2150 ± 0.002	0.0015
	40–50%	0.0911 ± 0.001	0.2150 ± 0.002	0.0015
	50–60%	0.0901 ± 0.003	0.1620 ± 0.005	0.0053
	60–70%	0.0880 ± 0.004	0.1330 ± 0.007	0.0100
	70–80%	0.0864 ± 0.010	0.1080 ± 0.016	0.0132
	80–92%	0.0787 ± 0.012	0.0864 ± 0.019	0.0152
Pb–Pb 2.76 TeV	0–5%	0.0993 ± 0.001	0.2890 ± 0.001	0.00098
	5–10%	0.0993 ± 0.001	0.2890 ± 0.001	0.00098
	10–20%	0.0993 ± 0.001	0.2890 ± 0.001	0.00098
	20–30%	0.0993 ± 0.001	0.2890 ± 0.001	0.00098
	30–40%	0.0993 ± 0.001	0.2890 ± 0.001	0.00098
	40–50%	0.0993 ± 0.001	0.2890 ± 0.001	0.00098
	50–60%	0.0904 ± 0.004	0.2582 ± 0.006	0.0052
	60–70%	0.0885 ± 0.004	0.2333 ± 0.006	0.0046
	70–80%	0.0882 ± 0.007	0.1988 ± 0.011	0.0092
	80–90%	0.0859 ± 0.010	0.1606 ± 0.020	0.0128

Table 3. Values of intercepts, slopes and χ^2 obtained from the linear fitting of $\langle p_T \rangle$ vs. $\bar{m}$ plot.

Collision	Centrality	Intercept	Slope	χ^2
Au–Au 200 GeV	0–5%	0.0815 ± 0.002	0.3340 ± 0.002	0.0018
	5–10%	0.0815 ± 0.002	0.3340 ± 0.002	0.0018
	10–15%	0.0815 ± 0.002	0.3340 ± 0.002	0.0018
	15–20%	0.0815 ± 0.002	0.3340 ± 0.002	0.0018
	20–30%	0.0815 ± 0.002	0.3340 ± 0.002	0.0018
	30–40%	0.0815 ± 0.002	0.3340 ± 0.002	0.0018
	40–50%	0.0815 ± 0.002	0.3340 ± 0.002	0.0018
	50–60%	0.0804 ± 0.002	0.3163 ± 0.002	0.0016
	60–70%	0.0799 ± 0.003	0.2946 ± 0.003	0.0024
	70–80%	0.0791 ± 0.008	0.2807 ± 0.009	0.0076
	80–92%	0.0763 ± 0.020	0.2572 ± 0.021	0.017

Table 3. *Cont.*

Collision	Centrality	Intercept	Slope	χ^2
Pb–Pb 2.76 TeV	0–5%	0.0900 ± 0.005	0.3487 ± 0.004	0.0044
	5–10%	0.0900 ± 0.005	0.3487 ± 0.004	0.0044
	10–20%	0.0900 ± 0.005	0.3487 ± 0.004	0.0044
	20–30%	0.0900 ± 0.005	0.3487 ± 0.004	0.0044
	30–40%	0.0900 ± 0.005	0.3487 ± 0.004	0.0044
	40–50%	0.0900 ± 0.005	0.3487 ± 0.004	0.0044
	50–60%	0.0831 ± 0.003	0.3420 ± 0.003	0.003
	60–70%	0.0723 ± 0.042	0.3352 ± 0.036	0.0382
	70–80%	0.0720 ± 0.026	0.3336 ± 0.024	0.0234
	80–90%	0.0717 ± 0.012	0.3072 ± 0.011	0.0101

We want to clarify that the transition from QGP to hadronic matter is seen to be estimated between 90 and 100 MeV in the present work, which is different from the values of lattice QCD and thermal and statistical models where the phase transition between QGP and hadronic matter occurs at 160 MeV [63–68], while according to Ref. [69], it occurs at 155 MeV. Ref. [70] shows the analysis based on finite size scaling and hydrodynamics, this temperature is 165 MeV, and the result from the realistic Polyakov–Nambo–Jona-Lasinio (rPNJL) model shows this temperature to be 93 MeV [71]. This is because different models have different thermometric scales. It is noteworthy that the initial and chemical freeze-out temperatures occur before the kinetic freeze-out temperature. The former occurs at the initial while the latter occurs at the intermediate stage of collisions, which is very helpful in the study of QGP. The temperature at the initial stages is so high that the matter created is far from equilibrium which, renders the temperature of the system to be not well-defined. Hence the temperature at the initial stages of collision may not be a good indicator of showing the phase transition. After a while, the particle yields become fixed at the stage of chemical freeze-out, and the chemical temperature is generally larger than the kinetic freeze-out temperature. Hence the chemical composition of the particles established before the kinetic freeze-out, and the phase transition may not be directly observed through the chemical freeze-out temperature. However, in the expansion of the fireball, the system cools down and reaches the stage of thermal freeze-out where the particles stop interacting. The particles follow a simple distribution during the kinetic freeze-out, which depends on temperature. The temperature extracted from such a distribution is believed to be close to the actual temperature of the particles at which the particles stop the interaction. We believe that the properties of the particles at the time of freeze-out are affected by the phase transition. For instance, if QGP is formed, it will affect how the quarks and gluons combine to form hadrons, which can give information about the properties of QGP.

Before heading toward the next section, we would like to comment that the present work could be more improved if we included the Higgs as well as top production, but unfortunately they are not presented in this study due to the reason that both the top quarks and Higgs particles are very massive particles, and their production is rare compared to the light particles, which makes it more challenging to detect and study. Furthermore, they have very short lifetimes and decay instantly after their production, and it is very difficult to identify or measure the decay products of these particles.

4. Summary and Conclusions

In this work, the transverse momentum (p_T) distributions of light and heavy particles in Au–Au and Pb–Pb collisions at $\sqrt{s_{NN}}$ = 200 GeV and $\sqrt{s_{NN}}$ = 2.76 TeV, respectively, are analyzed by a Tsallis–Pareto-type function which fits the experimental data well. Proton–proton collisions at the same colliding energy for the same particles are also analyzed in order to compare the thermodynamic nature of the two systems. We extracted the parameters T, q, T_0, β_T, N_0 and $\langle p_T \rangle$; T and q are extracted directly from the p_T spectra while T_0 and β_T are extracted from T by an alternative method. We reported that the trend

of T, T_0, β_T, $\langle p_T \rangle$ and q is the same and they are saturated in the central collisions up to 40 or 50% centrality, and beyond this, the former four parameters decrease while the latter one increases. This saturated trend shows the phase transition of QCD. The region in central collisions is meson-dominant while the peripheral collision region is baryon-dominant. The increase in temperature, flow velocity and the decrease in the entropy parameter from peripheral towards central collision are seen beyond the saturation region, which suggests that the peripheral collisions are far from equilibrium.

Additionally, the study of each particle with different T and q provides insights into the freeze-out process as the larger temperature and smaller q for the massive particles indicate that the massive particles freeze-out earlier than the lighter ones, and it reveals the multiple kinetic freeze-out scenario. The parameter N_0 is extracted and is reported to be decreasing towards the periphery which shows that the multiplicity decreases from central to peripheral collisions. All the above parameters have nearly the same values in p–p collisions to that in peripheral A–A collisions at the same colliding energy. We also reported the correlations among various parameters. The correlation of T and p_T, T and N_0, $\langle p_T \rangle$ and N_0 is positive, while that of T and q and $\langle p_T \rangle$ is negative.

Author Contributions: Conceptualization, A.H.I.; Methodology, A.H.I.; Software, M.B., M.A., E.A.D. and M.A.K.; Validation, A.H.I. and M.W.; Formal analysis, A.H.I., M.W. and M.U.M.; Investigation, M.B., A.H.I., M.W. and A.A.; Resources, M.B., A.H.I., M.A., M.U.M., E.A.D. and M.A.K.; Data curation, A.H.I.; Writing—original draft, A.H.I. and M.A.; Writing—review & editing, A.H.I. and M.W.; Visualization, A.H.I.; Supervision, A.H.I. and M.W.; Project administration, A.H.I.; Funding acquisition, A.H.I. All authors have read and agreed to the published version of the manuscript.

Funding: This research was funded by Ajman University, Internal Research Grant No.: [DRGS Ref. 2022-IRG-HBS-9].

Data Availability Statement: Not applicable.

Acknowledgments: We would like to acknowledge the support of Hubei University of Automotive Technology, and also the support of Ajman University, Internal Research Grant No.: [DRGS Ref. 2022-IRG-HBS-9].

Conflicts of Interest: The authors declare no conflict of interest.

Abbreviations

The following abbreviations are used in this manuscript:

p_T	transverse momentum
T_{eff}	kinetic freeze-out temperature
$\langle T_{eff} \rangle$	effective temperature
β_T	transverse flow velocity
$\langle \beta_T \rangle$	average transverse flow velocity
MC	Monte Carlo
LHC	Large Hadron Collider
N_{ch}	number of channels

References

1. Riordan, M. *The Hunting of the Quark: A True Story of Modern Physics*; Plunkett Lake Press: Lexington, MA, USA, 2019.
2. Ellis, J. The discovery of the gluon. *Int. J. Mod. Phys. A* **2014**, *29*, 1430072. [CrossRef]
3. Bass, S.A.; Gyulassy, M.; Stoecker, H.; Greiner, W. Signatures of quark-gluon plasma formation in high energy heavy-ion collisions: A critical review. *J. Phys. G Nucl. Part. Phys.* **1999**, *25*, R1–R57. [CrossRef]
4. Matsui, T.; Satz, H. J/ψ suppression by quark-gluon plasma formation. *Phys. Lett. B* **1986**, *178*, 416–422. [CrossRef]
5. Bialas, A.; Hwa, R.C. Intermittency parameters as a possible signal for quark-gluon plasma formation. *Phys. Lett. B* **1991**, *253*, 436–438. [CrossRef]
6. Liu, F.M.; Liu, S.X. Quark-gluon plasma formation time and direct photons from heavy ion collisions. *Phys. Rev. C* **2014**, *89*, 034906. [CrossRef]
7. Braun-Munzinger, P.; Stachel, J. The quest for the quark-gluon plasma. *Nature* **2007**, *448*, 302–309. [CrossRef]

8. Sanches, S.M., Jr.; Navarra, F.S.; Fogaça, D.A. The quark-gluon plasma equation of state and the expansion of the early Universe. *Nucl. Phys. A* **2015**, *937*, 1–16. [CrossRef]
9. Rafelski, J. Connecting QGP-heavy ion physics to the early universe. *Nucl. Phys. B-Proc. Suppl.* **2013**, *243*, 155–162. [CrossRef]
10. Kumar, Y.; Sharma, R.; Kuksal, G.; Jain, P.; Kumar, V.; Bangotra, P. Quark gluon plasma in the early universe expansion with quasi-particle approach. *J. Phys. Conf. Ser.* **2022**, *2349*, 012016. [CrossRef]
11. Sahoo, R.; Nayak, T.K. Possible early universe signals in proton collisions at the Large Hadron Collider. *arXiv* **2022**, arXiv:2201.00202.
12. Chen, C.H. Studying the Early Universe via Quark-Gluon Plasma. *Nucl. Phys. B-Proc. Suppl.* **2014**, *246*, 38–41. [CrossRef]
13. Heinz, U. The strongly coupled quark-gluon plasma created at RHIC. *J. Phys. A Math. Theor.* **2009**, *42*, 214003. [CrossRef]
14. Braun-Munzinger, P. Chemical equilibration and the hadron-QGP phase transition. *arXiv* **2000**, arXiv:nucl-ex/0007021.
15. Hirano, T.; Tsuda, K. Collective flow and two-pion correlations from a relativistic hydrodynamic model with early chemical freeze-out. *Phys. Rev. C* **2002**, *66*, 054905. [CrossRef]
16. Heinz, U.; Kestin, G. Universal chemical freeze-out as a phase transition signature. *arXiv* **2006**, arXiv:nucl-th/0612105.
17. Waqas, M.; Peng, G.X.; Liu, F.H.; Ajaz, M.; Haj Ismail, A.A.K. Investigation of the freeze-out parameters in B–B, O–O, Ca–Ca and Au–Au collisions at 39 GeV. *Eur. Phys. J. Plus* **2022**, *137*, 1026. [CrossRef]
18. Bass, S.A.; Dumitru, A. Dynamics of hot bulk QCD matter: From the quark-gluon plasma to hadronic freeze-out. *Phys. Rev. C* **2000**, *61*, 064909. [CrossRef]
19. Cleymans, J.; Hamar, G.; Levai, P.; Wheaton, S. Near-thermal equilibrium with Tsallis distributions in heavy-ion collisions. *J. Phys. G Nucl. Part. Phys.* **2009**, *36*, 064018. [CrossRef]
20. Shen, K.M.; Biro, T.S.; Wang, E.K. Different non-extensive models for heavy-ion collisions. *Phys. A Stat. Mech. Appl.* **2018**, *492*, 2353–2360. [CrossRef]
21. Osada, T.; Wilk, G. Non-extensive hydrodynamics for relativistic heavy-ion collisions. *Phys. Rev. C* **2008**, *77*, 044903. [CrossRef]
22. Alberico, W.M.; Lavagno, A. Non-extensive statistical effects in high-energy collisions. *Eur. Phys. J. A* **2009**, *40*, 313–323. [CrossRef]
23. Deb, S.; Sahu, D.; Sahoo, R.; Pradhan, A.K. Bose-Einstein condensation of pions in proton-proton collisions at the Large Hadron Collider using non-extensive Tsallis statistics. *Eur. Phys. J. A* **2021**, *57*, 158. [CrossRef]
24. Olimov, K.K.; Kanokova, S.Z.; Olimov, A.K.; Umarov, K.I.; Tukhtaev, B.J.; Gulamov, K.G.; Yuldashev, B.S.; Lutpullaev, S.L.; Saidkhanov, N.S.; Olimov, K.; et al. Combined analysis of midrapidity transverse momentum spectra of the charged pions and kaons, protons and antiprotons in $p+p$ and $Pb+Pb$ collisions at $\sqrt{s_{nn}}$ = 2.76 and 5.02 TeV at the LHC. *Mod. Phys. Lett. A* **2020**, *35*, 2050237. [CrossRef]
25. Cleymans, J.; Worku, D. Relativistic thermodynamics: Transverse momentum distributions in high-energy physics. *Eur. Phys. J. A* **2012**, *48*, 160. [CrossRef]
26. Schnedermann, E.; Sollfrank, J.; Heinz, U. Thermal phenomenology of hadrons from 200A GeV $S+S$ collisions. *Phys. Rev. C* **1993**, *48*, 2462. [CrossRef]
27. Abelev, B.I.; Aggarwal, M.M.; Ahammed, Z.; Alakhverdyants, A.V.; Anderson, B.D.; Arkhipkin, D.; Averichev, G.S.; Balewski, J.; Barannikova, O.; Barnby, L.S.; et al. Identified particle production, azimuthal anisotropy, and interferometry measurements in $Au+Au$ collisions at $\sqrt{s_{nn}}$ = 9.2 GeV. *Phys. Rev. C* **2010**, *81*, 024911. [CrossRef]
28. Abelev, B.I.; Aggarwal, M.M.; Ahammed, Z.; Anderson, B.D.; Arkhipkin, D.; Averichev, G.S.; Bai, Y.; Balewski, J.; Barannikova, O.; Barnby, L.S.; et al. Systematic measurements of identified particle spectra in pp, $d+Au$, and $Au+Au$ collisions at the STAR detector. *Phys. Rev. C* **2009**, *79*, 034909. [CrossRef]
29. Lao, H.L.; Liu, F.H.; Lacey, R.A. Extracting kinetic freeze-out temperature and radial flow velocity from an improved Tsallis distribution. *Eur. Phys. J. A* **2017**, *53*, 44. [CrossRef]
30. Tang, Z.; Xu, Y.; Ruan, L.; van Buren, G.; Wang, F.; Xu, Z. Spectra and radial flow in relativistic heavy ion collisions with Tsallis statistics in a blastwave description. *Phys. Rev. C* **2009**, *79*, 051901. [CrossRef]
31. Lao, H.L.; Wei, H.R.; Liu, F.H.; Lacey, R.A. An evidence of mass-dependent differential kinetic freeze-out scenario observed in Pb–Pb collisions at 2.76 TeV. *Eur. Phys. J. A* **2016**, *52*, 203. [CrossRef]
32. Lao, H.L.; Liu, F.H.; Li, B.C.; Duan, M.Y. Kinetic freeze-out temperatures in central and peripheral collisions: Which one is larger? *Nucl. Sci. Tech.* **2018**, *29*, 82. [CrossRef]
33. Wang, Q.; Liu, F.H. Initial and final state temperatures of antiproton emission sources in high energy collisions. *Int. J. Theor. Phys.* **2019**, *58*, 4119–4138. [CrossRef]
34. Bashir, I.U.; Uddin, S. Centrality Dependence of $K^*(892)^0$ and $\phi(1020)$ Production at LHC. *Commun. Theor. Phys.* **2017**, *68*, 500. [CrossRef]
35. Acharya, S.; Adamová, D.; Adhya, S.P.; Adler, A.; Adolfsson, J.; Aggarwal, M.M.; Rinella, G.A.; Agnello, M.; Agrawal, N.; Ahammed, Z.; et al. Production of charged pions, kaons, and (anti-) protons in Pb-Pb and inelastic pp collisions at $\sqrt{s_{NN}}$ = 5.02 TeV. *Phys. Rev. C* **2020**, *101*, 044907. [CrossRef]
36. Waqas, M.; Liu, F.H. Initial, effective, and kinetic freeze-out temperatures from transverse momentum spectra in high-energy proton (deuteron)–nucleus and nucleus-nucleus collisions. *Eur. Phys. J. Plus* **2020**, *135*, 147. [CrossRef]
37. Chatterjee, S.; Mohanty, B.; Singh, R. Freezeout hypersurface at energies available at the CERN Large Hadron Collider from particle spectra: Flavor and centrality dependence. *Phys. Rev. C* **2015**, *92*, 024917. [CrossRef]

38. Waqas, M.; Peng, G.X.; Ajaz, M.; Wazir, Z.; Haj, Ismail, A.A.K. Decoupling of non-strange, strange and multi-strange particles from the system in Cu–Cu, Au–Au and Pb–Pb collisions at high energies. *Chin. J. Phys.* **2022**, *77*, 1713–1722. [CrossRef]
39. Waqas, M.; Peng, G.X.; Liu, F.H.; Wazir, Z. Effects of coalescence and isospin symmetry on the freeze-out of light nuclei and their antiparticles. *Sci. Rep.* **2021**, *11*, 20252. [CrossRef]
40. Bíró, G.; Barnaföldi, G.G.; Biró, T.S. Tsallis-thermometer: A QGP indicator for large and small collisional systems. *J. Phys. G Nucl. Part. Phys.* **2020**, *47*, 105002. [CrossRef]
41. Su, Y.; Sun, Y.J.; Zhang, Y.F.; Chen, X.L. Non-extensive statistical distributions of charmed meson production in Pb–Pb and pp ($\overline{p}$) collisions. *Nucl. Sci. Tech.* **2021**, *32*, 108. [CrossRef]
42. Adler, S.S.; Afanasiev, S.; Aidala, C.; Ajitanand, N.N.; Akiba, Y.; Alexander, J.; Amirikas, R.; Aphecetche, L.; Aronson, S.H.; Averbeck, R.; et al. Identified charged particle spectra and yields in $Au + Au$ collisions at $\sqrt{s_{NN}}$ = 200 GeV. *Phys. Rev. C* **2004**, *69*, 034909. [CrossRef]
43. Adams, J.; Aggarwal, M.M.; Ahammed, Z.; Amonett, J.; Anderson, B.D.; Anderson, M.; Arkhipkin, D.; Averichev, G.S.; Bai, Y.; Balewski, J.; et al. Scaling properties of hyperon production in $Au + Au$ collisions at $\sqrt{s_{NN}}$ = 200 GeV. *Phys. Rev. Lett.* **2007**, *98*, 062301. [CrossRef] [PubMed]
44. ALICE Collaboration. Centrality dependence of ß, K, p production in Pb-Pb collisions at $\sqrt{s_{\mathrm{NN}}}$ = 2.76 TeV. *arXiv* **2013**, arXiv:1303.0737.
45. ALICE Collaboration. $\mathrm{K}^{0}_{\mathrm{S}}$ and Λ production in Pb-Pb collisions at $\sqrt{s_{\mathrm{NN}}}$ = 2.76 TeV. *arXiv* **2013**, arXiv:1307.5530.
46. ALICE Collaboration. Multi-strange baryon production at mid-rapidity in Pb-Pb collisions at $\sqrt{s_{\mathrm{NN}}}$ = 2.76 TeV. *arXiv* **2013**, arXiv:1307.5543.
47. STAR Collaboration. Identified hadron spectra at large transverse momentum in $p + p$ and $d + Au$ collisions at $\sqrt{s_{NN}}$ = 200 GeV. *arXiv* **2006**, arXiv:nucl-ex/0601033.
48. Abelev, B.; STAR Collaboration. Measurements of Strange Particle Production in $p + p$ Collisions at $\sqrt{s}$ = 200 GeV. *arXiv* **2006**, arXiv:nucl-ex/0607033.
49. The CMS Collaboration; Chatrchyan, S.; Khachatryan, V.; Sirunyan, A.M.; Tumasyan, A.; Adam, W.; Aguilo, E.; Bergauer, T.; Dragicevic, M.; Erö, J.; et al. Study of the inclusive production of charged pions, kaons, and protons in pp collisions at $\sqrt{s}$ = 0.9, 2.76, and 7 TeV. *Eur. Phys. J. C* **2012**, *72*, 2164. [CrossRef]
50. Li, L.L.; Liu, F.H.; Olimov, K.K. Excitation functions of Tsallis-like parameters in high-energy nucleus–nucleus collisions. *Entropy* **2021**, *23*, 478. [CrossRef] [PubMed]
51. Liu, L.; Yin, Z.B.; Zheng, L. Universal scaling of kinetic freeze-out parameters across different collision systems at LHC energies. *Chin. Phys. C* **2023**, *47*, 024103. [CrossRef]
52. Waqas, M.; Peng, G.X.; Ajaz, M.; Ismail, A.H.; Dawi, E.A. Analyses of the collective properties of hadronic matter in Au–Au collisions at 54.4 GeV. *Phys. Rev. D* **2022**, *106*, 075009. [CrossRef]
53. Che, G.; Gu, J.; Zhang, W.; Zheng, H. Identified particle spectra in Pb–Pb, Xe–Xe and p–Pb collisions with the Tsallis blast-wave model. *J. Phys. G Nucl. Part. Phys.* **2021**, *48*, 095103. [CrossRef]
54. Peng, G.X.; Waqas, M. Study of Proton, Deuteron, and Triton at 54.4 GeV (No. 2103.07852 v2). *Adv. High Energy Phys.* **2021**, *2021*, 6674470.
55. Chen, J.; Deng, J.; Tang, Z.; Xu, Z.; Yi, L. Nonequilibrium kinetic freeze-out properties in relativistic heavy ion collisions from energies employed at the RHIC beam energy scan to those available at the LHC. *Phys. Rev. C* **2021**, *104*, 034901. [CrossRef]
56. Waqas, M.; Peng, G.X.; Wazir, Z.; Lao, H.L. Analysis of kinetic freeze-out temperature and transverse flow velocity in nucleus–nucleus and proton–proton collisions at same center-of-mass energy. *Int. J. Mod. Phys. E* **2021**, *30*, 2150061. [CrossRef]
57. Barnby, L.; Bombara, M.; Burton, T.; Jones, P.; Nelson, J.; Timmins, A.; Abelev, B.I.; Elhalhuli, E. Systematic Measurements of Identified Particle Spectra in pp, d^{+} Au and Au+Au Collisions from STAR detector. *Phys. Rev. C* **2009**, *79*, 034909. [CrossRef]
58. Yang, P.P.; Duan, M.Y.; Liu, F.H. Dependence of related parameters on centrality and mass in a new treatment for transverse momentum spectra in high energy collisions. *Eur. Phys. J. A* **2021**, *57*, 63. [CrossRef]
59. Wei, H.R.; Liu, F.H.; Lacey, R.A. Disentangling random thermal motion of particles and collective expansion of source from transverse momentum spectra in high energy collisions. *J. Phys. G* **2016**, *43*, 125102. [CrossRef]
60. Takeuchi, S.; Murase, K.; Hirano, T.; Huovinen, P.; Nara, Y. Effects of hadronic rescattering on multistrange hadrons in high-energy nuclear collisions. *Phys. Rev. C* **2015**, *92*, 044907. [CrossRef]
61. Wei, H.R.; Liu, F.H.; Lacey, R.A. Kinetic freeze-out temperature and flow velocity extracted from transverse momentum spectra of final-state light flavor particles produced in collisions at RHIC and LHC. *Eur. Phys. J. A* **2016**, *52*, 102. [CrossRef]
62. Lao, H.L.; Liu, F.H.; Li, B.C.; Duan, M.Y.; Lacey, R.A. Examining the model dependence of the determination of kinetic freeze-out temperature and transverse flow velocity in small collision system. *Nucl. Sci. Tech.* **2018**, *29*, 164. [CrossRef]
63. Andronic, A.; Braun-Munzinger, P.; Stachel, J. The Horn, the hadron mass spectrum and the QCD phase diagram: The Statistical model of hadron production in central nucleus-nucleus collisions. *Nucl. Phys. A* **2010**, *834*, 237C–240C. [CrossRef]
64. Ratti, C. Lattice QCD and heavy ion collisions: A review of recent progress. *Rept. Prog. Phys.* **2018**, *81*, 084301. [CrossRef] [PubMed]
65. Datta, S.; Gavai, R.V.; Gupta, S. The QCD Critical Point: Marching towards continuum. *Nucl. Phys. A* **2013**, *904–905*, 883c–886c. [CrossRef]

66. Steinbrecher, P.; HotQCD Collaboration. The QCD crossover at zero and non-zero baryon densities from Lattice QCD. *Nucl. Phys. A* **2019**, *982*, 847–850. [CrossRef]
67. Cleymans, J.; Oeschler, H.; Redlich, K.; Wheaton, S. Comparison of chemical freeze-out criteria in heavy-ion collisions. *Phys. Rev. C* **2006**, *73*, 034905. [CrossRef]
68. Andronic, A.; Braun-Munzinger, P.; Stachel, J. Thermal hadron production in relativistic nuclear collisions. *Acta Phys. Polon. B* **2009**, *40*, 1005–1012.
69. Nonaka, C.; Asakawa, M. Hydrodynamical evolution near the QCD critical end point. *Phys. Rev. C* **2005**, *71*, 044904. [CrossRef]
70. Lacey, R.A. Indications for a Critical End Point in the Phase Diagram for Hot and Dense Nuclear Matter. *Phys. Rev. Lett.* **2015**, *114*, 142301. [CrossRef]
71. Xu, K.; Li, Z.; Huang, M. QCD critical end point from a realistic PNJL model. *EPJ Web Conf.* **2018**, *192*, 00019. [CrossRef]